2013

System Modeling and Optimization in Phase-Modulated Optical Fiber Communication Systems

Craig Huang
Minnesota State University - Mankato

System Modeling and Optimization in Phase-Modulated Optical Fiber Communication Systems

By

Craig Huang

A Thesis Submitted in Partial Fulfillment of the Requirements for
Master of Science
In
Electrical Engineering

Minnesota State University
Mankato, Minnesota

May 2013

Date:

This thesis paper has been examined and approved.

Examining Committee:

Dr. Qun Zhang, Chairperson

Dr. Muhammad Khaliq

Dr. Vincent Winstead

ACKNOWLEDGMENTS

I would like to express my sincerest gratitude to my advisor, Professor Qun Zhang, for his encouragement, guidance and support over the course of my graduate studies at Minnesota State University. Always genial and patient, his ever-cheery attitude has always been uplifting and a true delight. I would like to thank Dr. Muhammad Khaliq for his enlightening yet compliant advice and his inspiring vigor and passion during lectures that have been exceptionally edifying during my journey to discover my own niche in the field of Electrical Engineering.

I am also very grateful for Dr. Vincent Winstead's flexibility in his accommodation of my requests and needs over the past two years, including his willingness to serve on my defense committee on short notice. I must also thank Margaret Stoltzman for her cheery and pleasant manner that have made any administrative dealings stress-free and smooth. I am also grateful for all the knowledge imparted by the professors in the department I have had the pleasure to take courses with over the past two years.

I am very fortunate to have spent three semesters under the instruction of Dr. Ramakrishna Nair who, very sadly, is no longer with us. His teachings have formed a sizeable portion of the foundational curriculum I have received. I will always cherish his dry wit and endearing mannerisms.

Under no circumstances must the support of my peers be forgotten. The bond formed among academically embattled students striving to attain their respective degrees and

realize their dreams is one never broken. I thank my friends and classmates here at Minnesota State University as well as those from my time at the University of Minnesota for standing alongside me and instilling in me the spirit to fulfill my degree.

Last but not least, I am ever appreciative and blessed to have the unwavering support of my mother, father and brother. Their compassion throughout my years has been far more than I could have asked for. Without them, I would not be where I am today.

This thesis is dedicated to my loving parents and brother

TABLE OF CONTENTS

ABSTRACT

In this two-part study, the conclusions drawn from optimization of interferometer incoherent detection carried out by examining the effect of pre-emphasis within the electrical signal-driving path are examined first. This is an expansion upon a widespread industry standard as realized by the Oclaro group. System performance in tight optical filtering conditions can be improved with concurrent adjustments to the level of pre-emphasis and breadth of the delay-line interferometer free-spectral range. In the second study, we implement a dual-polarization quadrature phase-shift keyed modulation format with a digital signal processing block based upon the constant modulus algorithm realized via a feed-forward equalizer with and without the moving average method. Ultimately, the purpose of both studies is to study the efficacy of new modulation formats to enhance gains in spectral efficiency and improve robustness against chromatic dispersion within the optical fiber.

Chapter 1

Introduction to Optical Fiber Telecommunication Systems

1.1 INTRODUCTION

A variety of differing transmission media and technologies have been employed in recent years to support mobile and multimedia communications, enabling the near omnipresence of communications networks in the world today. Among them, fiber-optic systems are unrivaled in their low-loss, high bandwidth transmission capabilities across length spans when compared with free-space optics, radio and satellite transmission. As such, optical fiber communications have become an integral part of long-haul communications and the mainstay of interlinking wide area networks on both national and international scale. Furthermore, optical fiber communications are slowly permeating local area networks for provisional multimedia services.

In order to support the ever increasing demands of cellular and computer network capacity and reduce the network management complexity, researchers and companies alike have exerted concerted efforts towards the migration of system performance from 10 Gb/s and 40 Gb/s to 100 Gb/s per wavelength channel [1]. To better illustrate the growing demands, the the global IP traffic increase in backbone optical networks was estimated at 38% per year, corresponding to an approximate doubling per 26 months [2].

In a decade, an estimated 12X growth in global backbone traffic and corresponding capacity requisite in the span of the next decade [2]. It is quite clear that the roadmap for optical system advancement must be established with a definitive cognizance of network traffic evolution. In migrating to higher bitrate systems, networks will be better suited to load sharing and management by reducing the relative cost per bit transmitted.

Transoceanic fiber communications require amplifiers interspersed across the entire fiber length in order to counteract signal attenuation. As the input signal attenuates across a fiber span, optical amplifiers serve to exponentially increase signal power via stimulated photon emissions. Collision of the input signal Erbium ions within the amplifier results in emissions of duplicate photons as the ion returns to a low vibrational state [3]. However, stimulated emissions are also accompanied by spontaneous emissions of photons of random frequency and polarization states. As optical amplifiers are cascaded, these spontaneous emissions are also exponentially amplified with each additional span. The effect is amplified spontaneous emission (ASE) noise that pervades the signal at the receiver end and reduces the effective OSNR.

Legacy systems have implemented direction-detection schemes for commercial transceiver systems. However, since 2000, the paradigm has shifted away from purely intensity-modulated system into pseudo-multilevel modulation schemes utilizing a combination of intensity-modulation and phase modulation and onto coherent, entirely phase-modulated schemes to meet commercial performance demands [4]. The advantage of coherent schemes lies in their ability to eliminate chromatic dispersion (CD)

compensation using optical fiber. Rather, accumulated dispersion is compensated for within the receiver. Moreover, coherent schemes offer gains in either receiver sensitivity or spectral efficiency by upping the bit rate per physical spectral hertz.

Several motivations exist for this shift. Specifically, IM-DD systems, while simple to implement, exhibit lower bit error rate (BER) performance for the same optical SNR (i.e. inferior noise performance, low receiver sensitivity). With the progress in manufacturing processes in recent years, the emergence of DPSK systems with incoherent detection demonstrating higher receiver sensitivity in comparison with IM-DD offering greater noise tolerance, eliminating the number of optical amplifiers required along the length of a long haul fiber optic link which translates into cost saving for network infrastructure. However, further advancements in high-speed electronics and progress in digital signal processing (DSP) capabilities have pushed forth coherent schemes such as dual-polarization quadrature phase-shift keying (DP-QPSK) and quadrature amplitude modulation (QAM) systems demonstrating marked improvements in receiver sensitivity and greater spectral efficiency.

In our study, we review the performance of such legacy, purely intensity-modulated systems as well as a prior study here at Minnesota State University implementing a combinatory intensity- and phase-modulated scheme, carrier-suppressed return-to-zero format and conclude with the results of our simulation-based study implementing a coherent dual-polarization quadrature phase-shift keying modulation format for commercial applications.

1.2 INTENSITY-MODULATION DIRECT-DETECTION SYSTEMS

In optical communication systems, selection of an effective method to convert the electrical signal into an optical bit stream is critical. Generally, an optical source is modulated directly by the electrical signal or via an external modulator. The most rudimentary modulation technique to encode data over the optical carrier is the *on-off keying* (OOK) method. In this format, the optical bit stream conveys the information using two signal power levels with higher power representing information bit 1 and lower power representing 0. OOK systems employ *p-i-n* photodiodes in square-law detection. Like many other systems, OOK may be carried out in *nonreturn-to-zero* (NRZ) or *return-to-zero* (RZ) formats. For the NRZ format, the driving voltage will be NRZ. For the RZ format, an additional pulse-carving stage is necessary to return the driving voltage to zero to produce an RZ pulse in the optical domain. In the below Figures 1.1 and 1.2, the NRZ-OOK and RZ-OOK schemes for optical signal generation are illustrated, respectively.

In the RZ modulation format, a pulse representation of each 1-bit is shorter than the entirety of the bit duration [4]. For each 1-bit, the pulse returns to zero amplitude prior to the end of the bit duration. In the NRZ format, the pulse remains at '1' for adjacent 1-bits, contrary to the RZ format. As expected, the pulse width will vary depending upon the number of successive 1-bits adjacent to one another in the NRZ format. NRZ is advantageous when concerned with bandwidth limitations due to the absence of on-off transitions. The result of the NRZ format is bandwidth usage approximately half that of RZ. However, here, we are concerned with the RZ modulation.

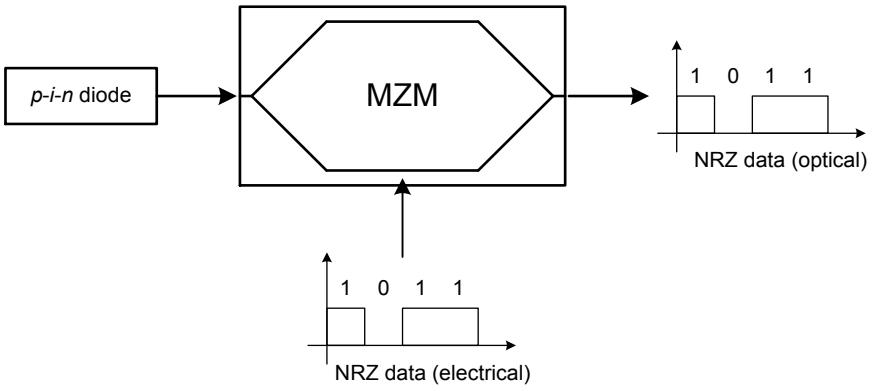

Figure 1.1. Block diagram for generation of NRZ-OOK optical signal

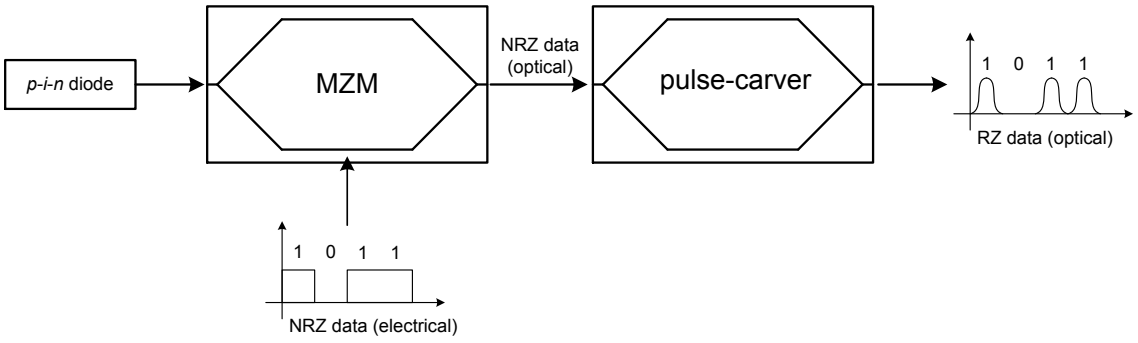

Figure 1.2. Block diagram for generation of RZ-OOK optical signal

The Mach-Zehnder modulator (MZM) employs an interferometer for the conversion of a phase shift into an amplitude modulation of the input continuous wave (CW) beam [4]. As illustrated in Figure 1.3 below of a $LiNbO_3$ MZM, voltage application to the contacts results in the conversion of the input CW signal into an encoded bit stream. At the input *Y* junction, A_i is divided into two equivalent parts and subsequently recombined at the output *Y* junction following the voltage-induced phase shifts at the contacts in each intermediate waveguide.

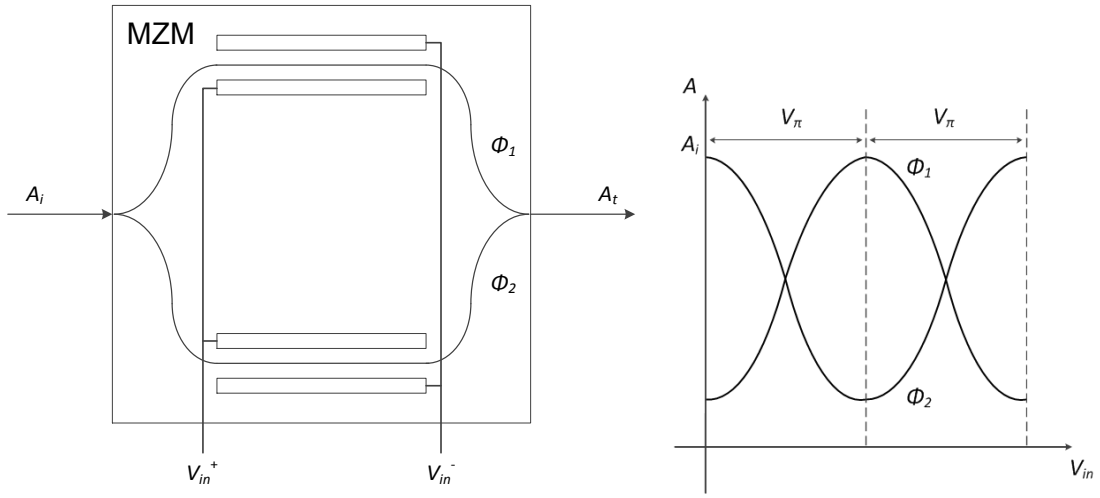

Figure 1.3. Mach-Zehnder modulator

The following expression delineates the phase shift imposed by the voltages spanning the waveguides [4]

$$\phi_j(t) = \frac{\pi V_j(t)}{V_\pi}$$

where

V_j : applied voltage across the *j*th waveguide

V_π : required voltage to induce a π phase difference

The V_π voltage is a known value specific to a particular $LiNbO_3$ MZM. With respect to the two phase shifts ϕ_1 and ϕ_2, the field transmission is defined as the following

$$A_t = \frac{1}{2} A_i \left(e^{i\phi_1} + e^{i\phi_2} \right)$$

where

ϕ_j : phase shift j = {1, 2}

A_i : input optical field

A_t : output optical field as defined by phase shifts ϕ_1 and ϕ_2

Usage of the RZ modulation format within the optical domain is primarily reserved for wavelength-division multiplexing (WDM) at 40 Gb/s or higher. The RZ format is useful in the resulting reduction of peak power due to pulse spreading. In addition, this pulse spreading effect results in the lessening of a number of nonlinear effects with adverse effects on system performance, yielding a greater resiliency than the NRZ format. However, for certain systems, the greater tolerance offered by RZ to nonlinearity is not readily apparent.

Harking back to Figures 1.1 and 1.2, the corresponding realizations of the NRZ-OOK and RZ-OOK optical signals using the MZM driver are illustrated in Figures 1.3 and 1.4. For the NRZ-OOK signal, the MZM is biased at 50% transmission to drive the peak-to-peak transmission with a V_π swing voltage. To generate the RZ-OOK signal, the same process is followed for NRZ-OOK prior to a second MZM acting as a pulse-carver as illustrated in Figure 1.2. The pulse width is drive at 50% of the bit duration with biasing of the push-pull MZM at the transmission midpoint as shown in Figure 1.4. The voltage swing of V_π is thus centered around 0 V, yielding a peak-to-peak of $-V_\pi/2$ to $+V_\pi/2$.

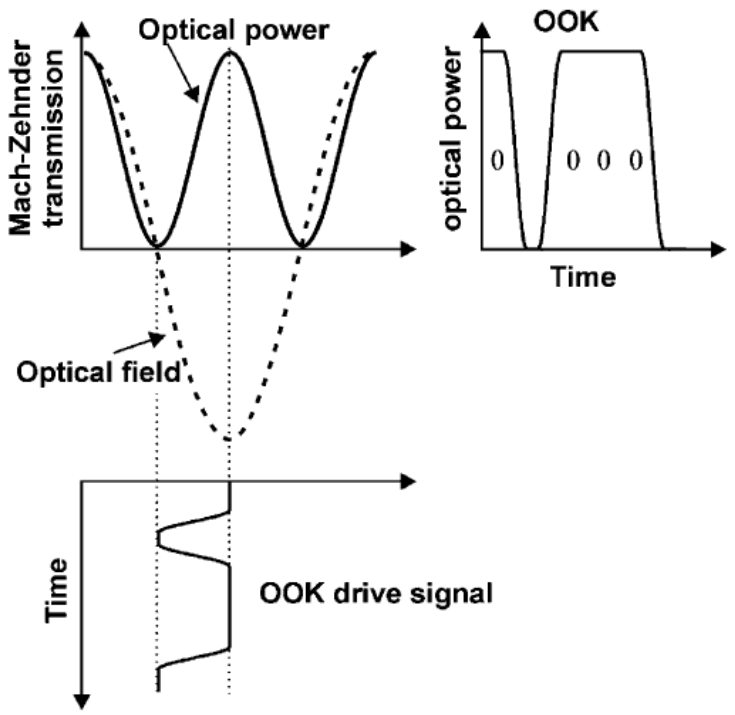

Figure 1.3. Driven MZM generation of NRZ-OOK optical signal [5]

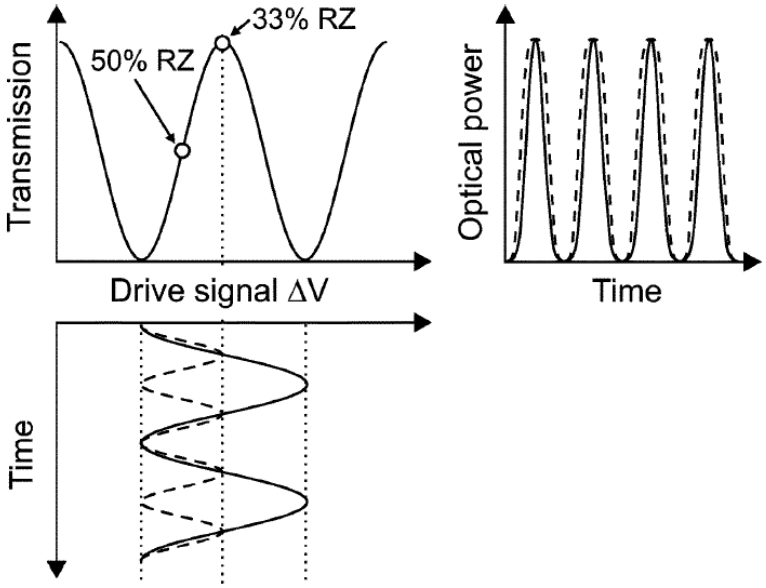

Figure 1.4. Drive MZM generation of RZ-OOK optical signal [6]

At present, the intensity-modulation, direct-detection (IM-DD) system, developed in 1978 for first-generational digital optical links, is most commonplace in existing fiber-

optic systems in the world. Use of intensity modulation scheme has more recently been bolstered by the development of erbium-doped fiber amplifiers (EDFA), allowing IM-DD scheme transmissions to attain performance approaching the quantum limit.

In the IM-DD scheme, the transmitted signal may be represented by $m(t)$. To evaluate the detected optical power P_o, we express P_o proportional to the signal amplitude power as adjusted by the modulation index γ as shown below

$$P_o = P_u[1 + \gamma \cdot m(t)]$$

where P_u is the mean received power and the expectation that $\gamma \cdot m(t) > -1$. With the mean received optical power, the detected mean square signal current is expressed as

$$\overline{I_s^2} = (RP_u\gamma)^2 \cdot \overline{m^2(t)}$$

where responsivity of the photodiode, R is

$$R = \frac{\eta q}{hv}$$

where η is the diode quantum efficiency, h is Planck's constant, q is the electrical charge, and v is the light frequency.

As we compare the merits of each additional modulation format in subsequent sections, a basic comparison that may be formed is the BER performance of each scheme. For the OOK format, the probability of bit-error is expressed as follows

$$P_b = Q\left(\sqrt{\frac{E_b}{N_0}}\right)$$

where

Q : complementary error function

E_b : energy-per-bit

N_0 : noise

As we consider the advantages of phase-modulation later on, we will see that the OOK format is at a 3 dB SNR disadvantage when compared to the binary and quadrature phase-shift keying formats. The corresponding BER for the binary and quadrature phase-shift keying formats is $P_b = Q\left(\sqrt{2\,E_b/N_0}\right)$. We will more thoroughly compare the intensity and phase modulation formats later on.

1.3 CARRIER-SUPPRESSED RETURN-TO-ZERO SYSTEMS

For higher performance systems, greater input power must be introduced in order to attain an equivalent average energy per bit to the power spectral density of ASE noise accrued as that observed in a slower system (i.e. 40 Gb/s versus 10 Gb/s). In order to achieve a greater input power, the modulation format implemented must be thoughtfully considered. However, the input power is capped by performance degradation attributed to the interaction between CD and Kerr nonlinearity. As such, methods to overcome

performance limitations posed by fiber nonlinearity are crucial as increasing system speeds are realized.

Previous studies have illustrated that the return-to-zero (RZ) modulation format exhibits greater resistance to fiber nonlinearity than the non-return-to-zero (NRZ) format [7]. To resist the effects of fiber nonlinearity, the pseudo-multilevel carrier-suppressed return-to-zero (CS-RZ) modulation scheme was introduced with the ability to accept even higher input signal power with respect to the RZ-OOK format. Given the ease of generating the CS-RZ format, this method has achieved widespread application [8].

In the CS-RZ format, the π phase difference between consecutive pulses results in the suppression of nonlinear interactions. Information is encoded on the intensity level with the phase altered by π for each bit without regard to the information transmitted. The occurrence of sign reversals for each bit transition is entirely independent of the carried information signal [6]. Effectively, the CS-RZ format yields less pulse distortion attributed to intra-channel nonlinear effects for the same input power. Greater input power is thus achieved by the CS-RZ format with respect to the RZ format.

In a prior study under Professor Zhang, a performance comparison study was conducted to evaluate the RZ and CS-RZ formats against one another. Using the Mach-Zehnder Modulator (MZM) in a push-pull configuration to generate a 67% duty-cycle, the CS-RZ modulation format is implemented by an input and output branch power division, yielding two optically induced phase shifts under the assumption of lossless coupling.

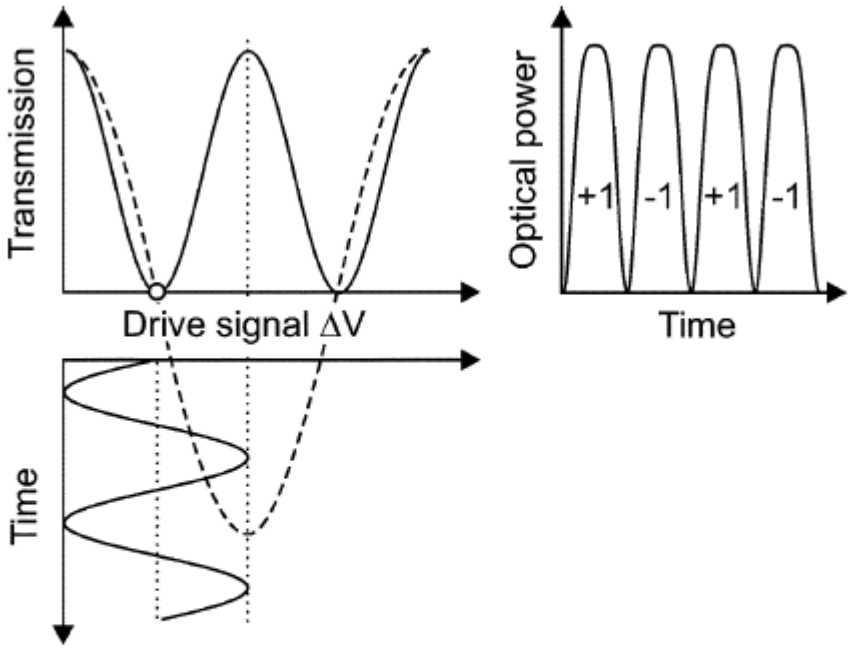

Figure 1.6 Realization of the CS-RZ signal [6]

Utilizing a cosine wave driving signal of 40 Gb/s for the RZ clock and 20 Gb/s driving signal for a 40 Gb/s CS-RZ clock, the simulation method utilized the *split-step Fourier* (SSF) and symmetric *split-step Fourier* (SSSF) methods to solve the *nonlinear Schrodinger Equation* (NLSE) and evaluate the RZ and CS-RZ formats. The pulse carver implementation of the MZM to produce a 67% duty-cycle CS-RZ may be visualized in the Figure 1.6.

In two varying simulations, one of a single 1545 nm channel across 1000 km transmission distance with variable inline dispersion compensation and the other with the aforementioned conditions and the inclusion of post-dispersion compensation, the CS-RZ

format outperformed RZ in large input power scenarios and equaled RZ in small input power without post-dispersion compensation. With post-dispersion over-compensation and low input power, the RZ format slightly outperforms CS-RZ. However, with or without post-dispersion compensation and low inline compensation, the CS-RZ format was found to have greater tolerance to intra-channel nonlinearity and mismatching inline compensation for low and high input power when compared to the RZ format.

In the CS-RZ regime, phase modulation is partially employed, but the scheme is still intensity modulated. More recently, purely phase-modulated formats have attracted due attention in response to the ability to improve WDM system spectral efficiency. In the next section, we discuss the implications of utilizing one phase-modulated encoding technique, differential binary phase shift keying (DPSK).

1.4 PHASE MODULATED SYSTEMS

The DPSK modulation format encodes bits via binary phase changes between adjacent bits. For example, a 1-bit is encoded upon a π phase change while no phase change is synonymous with a 0-bit. Similar to purely intensity modulated schemes, RZ and NRZ format implementations of DPSK are possible [6]. Unlike OOK, the receiver cannot use square-law detection due to the encoding of information into the optical signal phase, requiring the use of a delay-line interferometer (DLI) in the receiver.

The advantage of the DPSK format over direct-detection lies in its capability to surpass OOK on the part of 3-dB receiver sensitivity. This outcome may be understood in the

following Figure 1.7 which illustrates the corresponding $\sqrt{2}$ increase in symbol spacing for DPSK in comparison to a direct-detection modulation format. The $\sqrt{2}$ increase in symbol spacing for DPSK corresponds to improved robustness against optical field noise in comparison with OOK with identical BER [6].

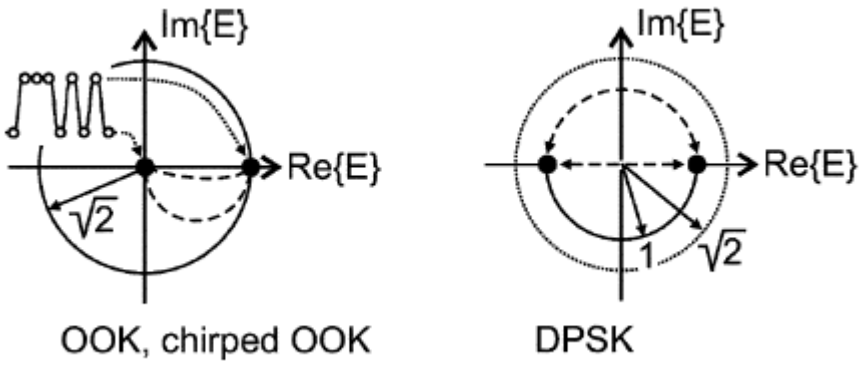

Figure 1.7. $\sqrt{2}$ increase in symbol spacing from DPSK to OOK (purely intensity-modulated) [6]

To realize the DPSK scheme, the optical transmitter differentially encodes the signal to circumvent error propagation attributed to receiver-end differential decoding. The differential nature of the signal is brought about via signal precoding, where the phase difference between subsequent bits is characterized as 0 or 1 in relation to unchanging or changing adjacent bit values, respectively. Following precoding, the laser source optical field phase is switched between 0 and π in relation to the bit sequence to be transmitted. Once again, an MZM is used to carry out the optical phase modulation. The MZM is driven symmetrically about zero transmission, modulating the signal by transitions along the real axis as visualized in Figure 1.7 [6]. The result of this modulation across the real

axis is precise π phase variation at the cost of loss of optical intensity at the site of the phase transition. The DPSK system scheme is represented in Figure 1.8. However, this deviation in optical intensity is not of significant concern while implementing DPSK. Rather, DPSK requires exact phase modulation as opposed to maintenance of consistent optical intensity.

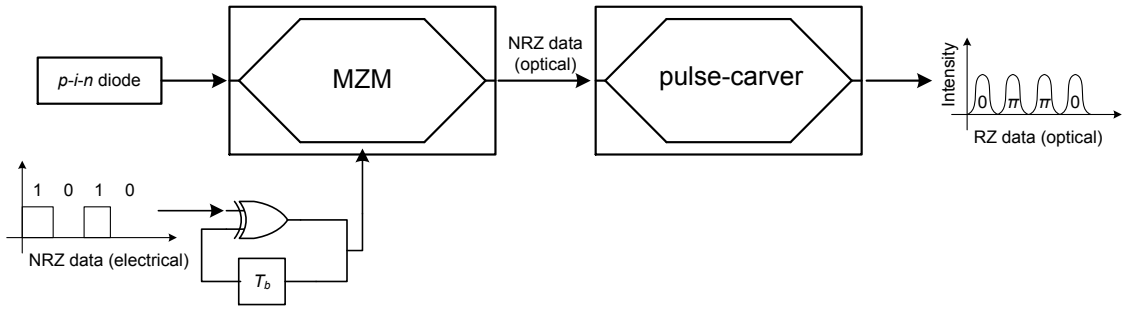

Figure 1.8. Block diagram of RZ-DPSK optical signal generation scheme

The DPSK modulated signal cannot be received directly by means of square-law detection. Conversion of differential phase modulated signal into an intensity modulated format is brought about using a delay line interferometer (DLI) to effectually demodulate the signal. The DLI divides the signal into two paths with a delay equivalent to one bit duration. Thus, at the DLI output, interference of the previous and present bits will yield either constructive or destructive interference. If a phase change does not exist between the differentially delayed bits, combination of the two optical fields at the DLI output results in destruction interference. Conversely, should a phase difference between adjacent bits, the DLI output will produce a constructive interference. In this way, the DLI operates in agreement with the differential precoding.

A direct comparison between DPSK and intensity modulation demonstrates substantial reduction in the system OSNR requirement. In general, gain of balanced-detection DPSK is not dependent upon target BER, leading to a difference of approximately 3 dB in savings for OSNR requirements of RZ-DPSK over RZ-OOK at BER 1e-3 in a back-to-back system scheme [6]. This discrepancy only favors DPSK with a greater number of optical add-drop multiplexer (OADM) sites.

DPSK allows for constant amplitude, returning constant average power or constant SNR. Thus, the peak average power is reduced as compared to OOK formats. This in turn alleviates nonlinear penalties associated with fiber imperfections. At present, DPSK systems have proven effective in commercial systems [9]. However, DPSK modulation is still a form of incoherent detection. Coherent systems previously garnered interest, but the feasibility of these systems in practice was limited by the difficulty and complexity involved in effecting electronic or DSP techniques on the receiver end to exploit optical phase information.

In recent years, coherent detection BPSK and QPSK systems have been studied, yielding a significant advancement in system complexity [10]. To maximize spectral efficiency, BPSK is not preferred due to the binary signaling nature of the format. Rather, to maximize the number of bits encoded per hertz of the spectral rate of transmission, studies have overlooked the BPSK format to research polarization multiplexed QPSK systems due to the identical receiver sensitivity but doubled spectral efficiency of QPSK over BPSK (with grey-coding). Furthermore, the dual polarization nature of polarization-

multiplexed QPSK enables double the channel capacity when compared with BPSK. The details of this transceiver structure are expounded in Chapter 3.

1.5 THESIS MOTIVATION AND ORGANIZATION

In the previous work, techniques to optimize DPSK transceivers with interferometer incoherent detection have been extensively explored [11, 12]. In [12], an 80 Gb/s NRZ-DPSK transceiver was optimized by means of pre-emphasis within the electrical signal driving path. Recently, the Oclaro group proposed a scheme that can enhance the DPSK transceiver performance under tight optical filtering conditions. In [11], optimization of a 44 Gb/s RZ partial DPSK (PDPSK) transceiver was carried out by pre-emphasis within the electrical signal driving path and the additional inclusion of adjustments to the DLI free spectral range to further boost performance. Previous systems have used the NRZ format without pre-emphasis. Co-optimization of FSR and pre-emphasis for the RZ-PDPSK format was demonstrated to confer enhanced BER performance in strong filtering conditions synonymous with long haul communications requiring multiple OADM sites. The results of this study are explicated in Chapter 2.

While popular in past commercial implementations, legacy systems based upon OOK formats are being phased out in favor of phase modulated systems in order to improve spectral efficiency. Furthermore, coherent detection systems are in demand due to the ability to sort out the complexities associated with coherent, phase-modulate schemes on the receiver end [9]. Our group has been developing a simulation environment to model

the newly emerging phase-modulated optical fiber communication systems with coherent detection.

Coherent signal transmission systems offer three primary advantages over direct-detection implementations [13]. Namely,

1) OOK or direct-detection systems are limited to intensity modulation while coherent systems allow phase modulation formats that could lead to receiver sensitivity enhancement with coherent detection.
2) The essence of being a linear system enables coherent systems to utilize the dual polarizations to double the channel capacity
3) High frequency selectivity is possible with post-detection filtering within the optical domain, permitting high-density WDM schemes

In our study, implementation of DP-QPSK creates four distinct carrier phase values 0, $\pi/2$, π, and $3\pi/2$, improving spectral efficiency over IM-DD by simultaneous transmission of four bits. Thus the effective bit rate, or symbol rate, is halved. Nonetheless, improvements to spectral efficiency have their accompanying difficulties. In particular, coherent systems require complex receiver schemes in order to retrieve the polarization-multiplexed phase-encoded information within the optical carrier signal. Fortunately, recent progress in high speed analog circuits and digital microelectronics enables high speed DSPs that are essential to handle the receiver signal processing tasks.

Several obstacles must be overcome in order to achieve acceptable system performance in coherent transceiver schemes, namely, ASE, CD, polarization-mode dispersion (PMD), and fiber Kerr nonlinearity. Given the polarization multiplexing nature of DP-QPSK, mixing between the two states of polarization (SOP) over the course of the fiber channel eventually render the simultaneously transmitted signals indistinguishable. Here, we are particularly interested in alleviating CD and PMD induced penalties in recovery of the two original states of polarization by means of implementing the constant-modulus algorithm with feed-forward equalization to enable transceiver adaptation to variable fiber birefringence.

In the next chapter, discussion of the results of an incoherent RZ-PDPSK transceiver scheme and identification the advantages to allowing adjustment to the level of electrical drive signal pre-emphasis and selection of DLI FSR to complement system performance under different degrees of optical filtering strength are covered at length in Chapter 2. The course of discussion then turns to the modeling of a coherent DP-QPSK transceiver scheme using a complex DSP scheme for dual SOP recovery following fiber transmission in Chapter 3. The subsequence discourse is focused upon summary of the results of these two studies and the future direction of research in achieving the next-generation fiber optic system specifications in Chapter 4 to conclude the content of this thesis.

Chapter 2

Performance Optimization of Differential Phase-Shift Keying Systems

2.1 RETURN-TO-ZERO DPSK TRANSCEIVER MODEL

In the continual overhaul of present optical transmission systems to counter the growth of multimedia communications, the expected shortening of optical pulses associated with higher transmission speeds poses a significant obstacle to increasing or sustaining present system performance. With the shift of present OOK-based 10 Gb/s system to 40 Gb/s systems, For a back-to-back system neglecting fiber channel effects, the average optical signal power must be increased fourfold in order to maintain a 0.1 nm OSNR and match the OOK-based system performance. 0.1 nm OSNR corresponds to the ratio of total signal power to optical amplifier noise power for 0.1 nm bandwidth. However, a fourfold increase in signal power leads to a substantial increase in nonlinear interference associated with fiber nonlinearity amid optical signals. Without combating the detrimental effects of accumulated noise, the system performance will suffer.

Here, we present the popularized solution, a balanced, noncoherent binary DPSK modulation system implementation, facilitating the deployment of 40 Gb/s systems. As we discussed previously, DPSK schemes employing balanced detection are markedly superior to IM-DD concerning system resiliency to optical noise. However, the wide

signal spectra associated with the RZ-DPSK limits spectral efficiency. Moreover, the application of these schemes in long haul terrestrial communications has led to a steady increase in the number of OADM sites. As such, the aggregate effect of filter cascading and detuning produces strong optical filtering, introducing inter-symbol interference (ISI) that corrupts system performance to a great degree.

In our study, we wish to determine the BER performance of an RZ-DPSK system. To evaluate BER of the system in its entirety, a quasi-analytical (QA) method based upon the Karhunen-Loève series expansion (KLSE) is used [14]. We implement the QA method in a numerical MATLAB simulation environment. To evaluate the RZ-DPSK system, a pseudo-random bit sequence (PRBS) must first be generated. A rigorous DPSK transceiver model was previously developed for this express purpose. The transceiver model is shown in the below Figure 2.1.

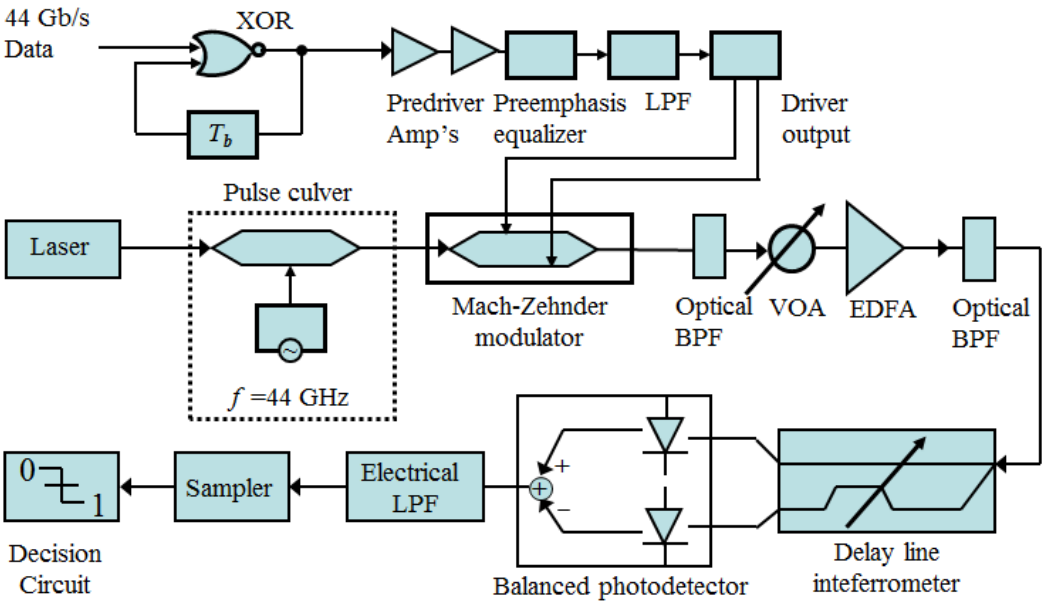

Figure 2.1. Optical RZ-DPSK transceiver model

As illustrated in the figure, 44 Gb/s NRZ data enters a differential encoding block where the present bit is combined in XOR logic with the previous bit (by means of a one bit period delay, 'T_b') to produce a DPSK-encoded signal. The encoded signal then passes through a high gain multi-stage predriver amplifier at a 3 dB bandwidth of 32 GHz. As the passes through a linear-phase pre-emphasis block, high frequency components of the electrical signal are pre-emphasized. The linear-phase assumption applies singularly to the pre-emphasis circuit in order to properly evaluate the pure-bandwidth effect. This signal is then passed through a 5^{th} order Bessel low-pass filter (LPF). We present the result of differing pre-emphasis levels in a later chapter. A push-pull MZM with a 3dB bandwidth of 30 GHz is employed to satisfy the requirement of a large driving signal.

In Figure 2.1, the optical source, a single frequency laser with negligible line width, generates CW light. The CW light passes through a periodic pulse driven MZM acting as a pulse carver. The driving pulse may be characterized as voltage, $V(t)$, represented in the following expression

$$V(t) = V_1 \cos(2\pi f_1 t) + V_{\text{bias}}$$

where

V_1 : pre-emphasized voltage component of driving signal $V(t)$

V_{bias} : bias voltage for pulse carving

f_1 : driving pulse frequency

V_{bias} is preferentially set at $V_\pi/2$ with driving pulse frequency f_1 set to the data rate. In addition, the peak-to-peak driving pulse voltage swing is set to $V_\pi/2$. Let $E_0(t)$ represent the optical field complex envelope at the pulse carver input. The signal complex envelope at the output of the pulse carver is then expressed as

$$E_{\text{carved}}(t) = \frac{E_0(t)}{2}\left[\gamma e^{\frac{j\pi V(t)}{V_\pi}} + 1\right]$$

$$\gamma = \frac{\sqrt{\delta} - 1}{\sqrt{\delta} + 1}$$

where δ is the modulator linear intrinsic intensity extinction ratio.

The MZM in push-pull configuration following the pulse carver phase modulates the signal. The driver pulse is represented as voltages $V_1(t)$ and $V_2(t)$. MZM output $E_{\text{mzm}}(t)$ is defined as follows

$$E_{\text{mzm}}(t) = \frac{E_{\text{carved}}}{2}\left[e^{\frac{j\pi R_0(f)H_e(f)V_1(t)}{V_\pi}} + \gamma e^{\frac{j\pi R_0(f)H_e(f)V_2(t)}{V_\pi}}\right]$$

where

$R(f)$: modulation frequency response

$H_e(f)$: combined frequency response of the driving circuits

$R(f)H_e(f)V_j(t)$: IFT[$R(f)H_e(f)$FT[$V_j(t)$]] where j = {1, 2} and FT and IFT are the Fourier transform (FT) and inverse FT, respectively

The optical signal passes through a 2nd order super-Gaussian-shaped optical band-pass filter (BPF). In our transceiver model, the BPF takes on two different 3 dB FWHM bandwidths. We will examine the implications of the bandwidth selection in a later

chapter. Inclusion of a variable optical attenuator (VOA) mimics the signal power loss that occurs over a real optical channel by controlling the launch power, and an EDFA model introduces optical amplified noise. The transceiver is modeled with a constant noise figure. The accumulated spontaneous emission (ASE) and EDFA noise are characterized as additive white Gaussian noise (AWGN) in the simulation environment.

At the receiver end of the system, the optical signal passes through a second optical BPF identical to the first. The signal is then demodulated by the DLI and enters a balanced photodetector to convert the optical signal to an electrical signal once more. The electrical signal then proceeds through a sampler and decision circuit to ensure correct detection.

Returning to our prior discussion of the BER calculation, we employ the QA method due to the inability for a comprehensive mathematical analysis of the transceiver system due fiber nonlinearity. We account for the effect of PRBS length by using a 16-bit De Bruijn sequence. The De Bruijn sequence encompasses all 4-bit patterns with precisely one occurrence of each pattern. By conceiving a sequence of sampling time $\{T_k\}$, a set of probability distribution functions (pdf) $f_y(y,T_k)$ may be attained based upon the detected marks and spaces.

By the KLSE-based QA method, we examine the signal after demodulation and conversion to the electrical domain following the DLI and balanced photodetector. As a result of the DLI, the obtained voltage $V(t)$ maybe expressed as

$$V(t) = V_s(t) - V_d(t)$$

where $V_s(t)$ and $V_d(t)$ are the sum and difference branch voltages, respectively. The constructive and destructive portions of the signal following the photodetector are represented by

$$V_s(t) = \sum_{k,l=-N/2}^{N/2-1} (A_k + a_k)^* H_o(\omega_k)^* H_s(\omega_k)^* (A_l + a_l) H_o(\omega_l) H_s(\omega_l) e^{j(\omega_l - \omega_k)t}$$

$$= \sum_{k,l=-N/2}^{N/2-1} (A_k + a_k)^* H_{os}(\omega_k)^* (A_l + a_l) H_{os}(\omega_l) e^{j(\omega_l - \omega_k)t}$$

$$V_d(t) = \sum_{k,l=-N/2}^{N/2-1} (A_k + a_k)^* H_o(\omega_k)^* H_d(\omega_k)^* (A_l + a_l) H_o(\omega_l) H_d(\omega_l) e^{j(\omega_l - \omega_k)t}$$

$$= \sum_{k,l=-N/2}^{N/2-1} (A_k + a_k)^* H_{od}(\omega_k)^* (A_l + a_l) H_{od}(\omega_l) e^{j(\omega_l - \omega_k)t}$$

where

$H_s(\omega)$: sum branch transfer function

$H_d(\omega)$: difference branch transfer function

$H_o(\omega)$: optical BPF transfer function

* : complex conjugate operation

The electrical LPF voltage output $y(t)$ is modeled with impulse response $f(t)$ in the following expression

$$y(t) = \int_{-\infty}^{t} f(t-\tau)V(\tau)d\tau = \int_{-\infty}^{\infty} f(t-\tau)V(\tau)d\tau$$

$$= (A_k + a_k)^*[H_{os}(\omega_k)^* W_{kl}(t) H_{os}(\omega_l) - H_{od}(\omega_k)^* W_{kl}(t) H_{od}(\omega_l)](A_l + a_l)$$

$$W_{kl}(t) = e^{j(\omega_l - \omega_k)t} \int_{-\infty}^{\infty} f(t-\tau)e^{-j(\omega_l-\omega_k)(t-\tau)}d\tau$$

$$= e^{j(\omega_l-\omega_k)t} F_{kl}$$

where

F_{kl} = FT[$f(t)$] evaluated at $\omega_l - \omega_k$

Expression of $y(t)$ in matrix form yields

$$y(t) = (A + a)^H \left(\mathrm{H}_{os}{}^H \mathrm{W} \mathrm{H}_{os} - \mathrm{H}_{od}{}^H \mathrm{W} \mathrm{H}_{od}\right)(A + a)$$

$$= (A + a)^H \widetilde{\mathrm{W}} (A + a)$$

where

$(\cdot)^H$: complex conjugate and transpose operation

$A = \left(A_{-N/2}, \ldots A_{N/2-1}\right)^T$

$a = \left(a_{-N/2}, \ldots a_{N/2-1}\right)^T$

$\mathrm{H}_{os} = \mathrm{diag}\left(H_{os}\left(\omega_{-N/2}\right), \ldots H_{os}\left(\omega_{N/2-1}\right)\right)$

$\mathrm{H}_{od} = \mathrm{diag}\left(H_{od}\left(\omega_{-N/2}\right), \ldots H_{od}\left(\omega_{N/2-1}\right)\right)$

$\widetilde{\mathrm{W}} = \mathrm{H}_{os}{}^H \mathrm{W} \mathrm{H}_{os} - \mathrm{H}_{od}{}^H \mathrm{W} \mathrm{H}_{od}$

The limitations imposed by the self-phase modulation (SPM) resulting in nonlinearity prevents the use of in- and out-of-phase noise components. Instead, the real and imaginary noise components are used. Here, we do not show the partitioned vector expressions of A and a, the information and noise components of the signal, respectively. The vector expressions are more thoroughly detailed in the dissertation of Akhlaqur Rahman. Here, we are expressly interested in the outcome following application of the diagonalization theorem in order to derive the set of pdf's. The Karhunen-Loeve modes Q_k and q_k for signal and noise, respectively, are a result of the transformation performed to solve the diagonalization operation. The received signal $y(t)$ may thus be represented as follows

$$y(t) = (Q+q)^T \Lambda (Q+q)$$

$$= \sum_{k=1}^{2N} \lambda_k \left({Q_k}^2 + 2Q_k q_k + {q_k}^2 \right)$$

$$= \sum_{k=1}^{2N} g_k(q_k)$$

where

$\Lambda = \text{diag}(\lambda_1, \lambda_2, \ldots \lambda_N)$ with real λ_k

g_k : new set of random variables

The characteristic function for $y(t)$ follows the derivation detailed in Appendix B of Rahman's dissertation. Here, we show the characteristic function to better illustrate the relation between the received voltage output and its relation with the final pdf, $f_y(y)$.

$$\Phi_y(\zeta, t) = \prod_{k=1}^{2N} \langle \exp(i\zeta g_k) \rangle$$

$$= \prod_{k=1}^{2N} \int_{-\infty}^{\infty} \exp[i\zeta g_k(q_k)] f_{qk} dq_k$$

As the noise modes q_k are independent and identically distributed random variables with zero mean and unit variance, the resulting characteristic equation is as follows

$$\Phi_y(\zeta, t) = \prod_{k=1}^{2N} \frac{1}{\sqrt{1 - 2i\lambda_k\zeta}} \exp\left(-\frac{2{\lambda_k}^2 {Q_k}^2 \zeta^2}{1 - 2i\lambda_k\zeta} + i\lambda_k {Q_k}^2 \zeta \right)$$

The above expression consists of all real variables. The first term within the exponential models the signal-noise beat influence, and the second term within the exponential mimics the receiver noise-noise beat. Thus, the desired pdf $f_y(y)$ is expressed as follows

$$f_y(y, T_k) = \frac{1}{2\pi} \int_{-\infty}^{\infty} \Phi_y(\zeta, t) \exp(iy\zeta)\, d\zeta$$

Thus, with knowledge of the distinct pdf's, we may now ascertain the minimum system BER. With the set of pdf's, the optimal BER may be determined by finding the minimum of the average for each pdf. The BER is expressed as follows

$$\text{BER} = \min |_{\gamma_{th}} \text{Avg}_{pdf}[P_e(\gamma_{th};\ pdf)]$$

where

γ_{th} : detection threshold

P_e : probability of error

pdf : set of pdf's for the detected marks and spaces

With the above expression, we may effectively evaluate the overall system BER for all marks and spaces. The minimum BER value corresponds to the optimal decision level determined by the pdf's.

2.2 RZ-DPSK SYSTEM SIMULATION AND RESULTS

In our simulation model, we use a RZ partial DPSK (PDPSK) rather than a straightforward RZ-DPSK scheme. The so-called PDPSK scheme allows for optimization of system performance under stronger filtering conditions. Thus, in our study, we consider two differing system setups, one where the transceiver operates under a baseline filtering condition with the 3 dB bandwidth set to 63.0 GHz. The strong filtering condition is set to a combined 3 dB bandwidth of 37.5 GHz. To augment system performance, pre-emphasis of the signal high frequency range and variations to the free spectral range (FSR) of the DLI are investigated. The result of using these different system parameters is reviewed later on within this subsection.

As described earlier, a PRBS is generated and passed through the transceiver system. In the following figure, we show a short 8-bit sequence in order to illustrate the progression of the signal through the encoder and MZM immediately preceding transmission. Adhering to the differential requirement of DPSK modulation, the encoding produces the bit sequence corresponding to phase changes.

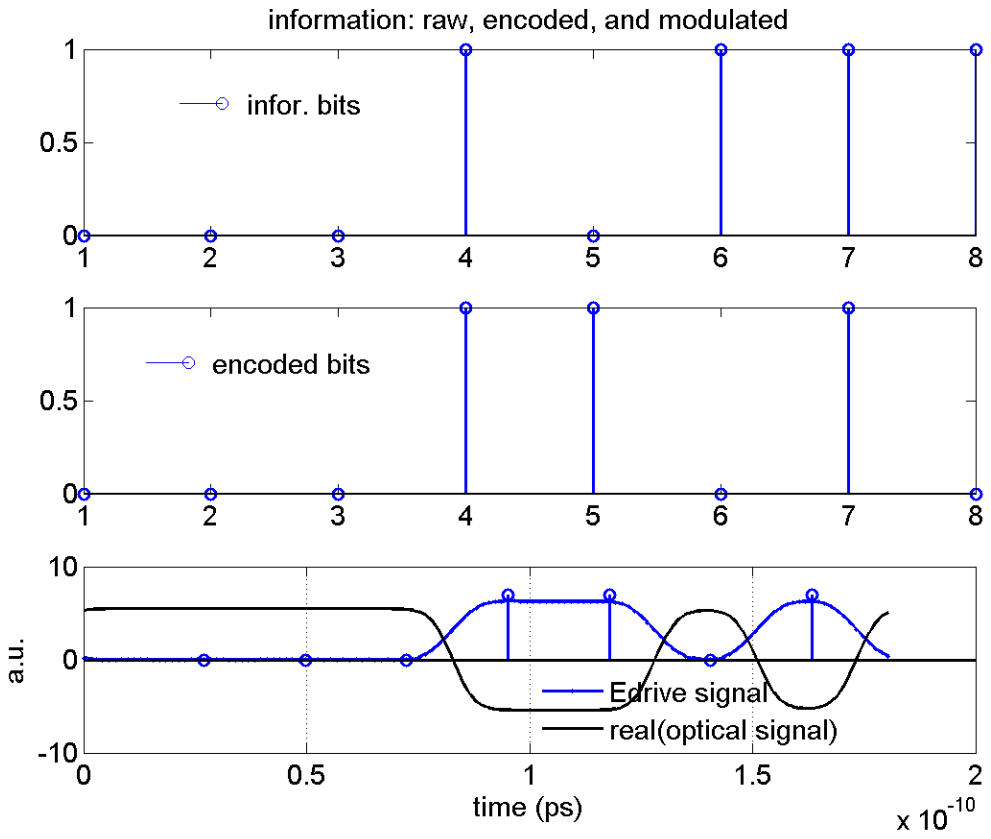

Figure 2.1. Raw, encoded and Mach-Zehnder modulated signals from top to bottom, respectively

Note that when the electrical drive signal voltage is delivered to the MZM, the optical signal is effectively the inversion of the drive signal. The electrical signal begins as trapezoidal-shaped RZ data with a rise and fall time of 12 ps. This RZ data is represented in the following Figure 2.2 below

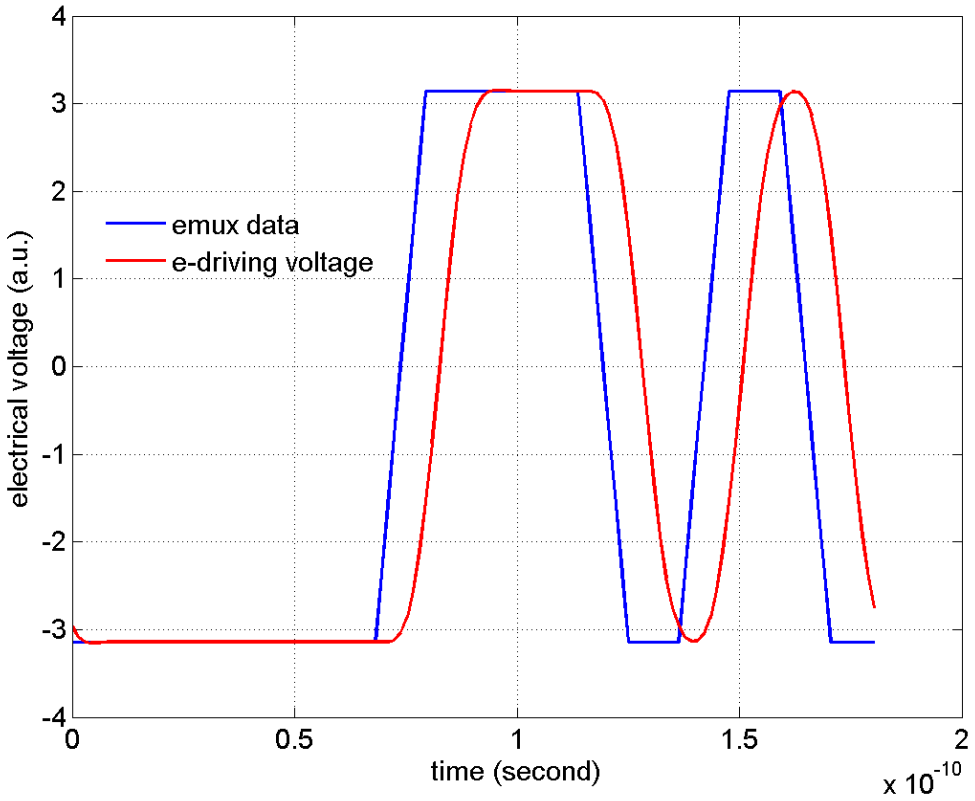

Figure 2.2. The electrical multiplexer data and electrical driving voltage compared

As mentioned earlier, a variation to the DPSK format, PDPSK, is implemented to provide optimal filter performance. As proposed by Tibuleac and Filer [15], DLI bandwidth tuning at the receiver end, or FSR, may optimize system performance with strong filtering. Strong filtering is imposed upon the system by means of two comparative levels of inline optical filtering. The baseline scenario features a 3dB bandwidth of 63.0 GHz inline filtering, while the strong filtering scenario is set at 37.5 GHz. To test the FSR effects, the relative delay between the two respective interferometer arms is adjusted with differing bandwidth values ranging between 44 GHz to 68 GHz at 4 GHz. The second aspect investigated is the resultant effect of pre-emphasis of the high frequency range on

system performance when implemented in the electrical driving path. Five differing levels of pre-emphasis are tested and compared to the case with no pre-emphasis. The transfer functions of these five pre-emphasis levels are shown in Figure 2.3.

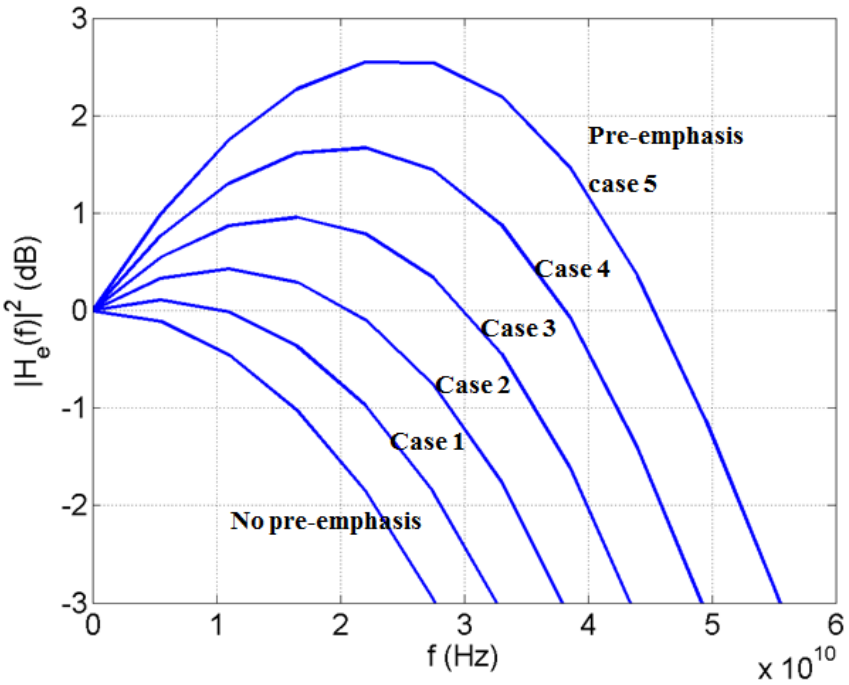

Figure 2.3. Frequency response for no pre-emphasis and five varying levels of pre-emphasis (driving path frequency response absolute value squared versus frequency)

At the baseline filtering level, a series of 1024 optical pulses are transmitted, and the resulting eye diagram for these pulses prior to passing through the first optical BPF is plotted for no pre-emphasis, case 3 and case 5 pre-emphasis levels. With no pre-emphasis, diminished system performance is attributed to the transmitter bandwidth limitations. However, in pre-emphasis case 5, pre-emphasizing high frequencies to too great a degree also results in degraded eye performance as well. As is shown in Figure 2.4, pre-

emphasis case 3, corresponding to a driving circuit 3 dB bandwidth of 32.5 GHz, produces the best eye opening, striking a happy medium between no pre-emphasis and the highest degree of pre-emphasis examined in this study.

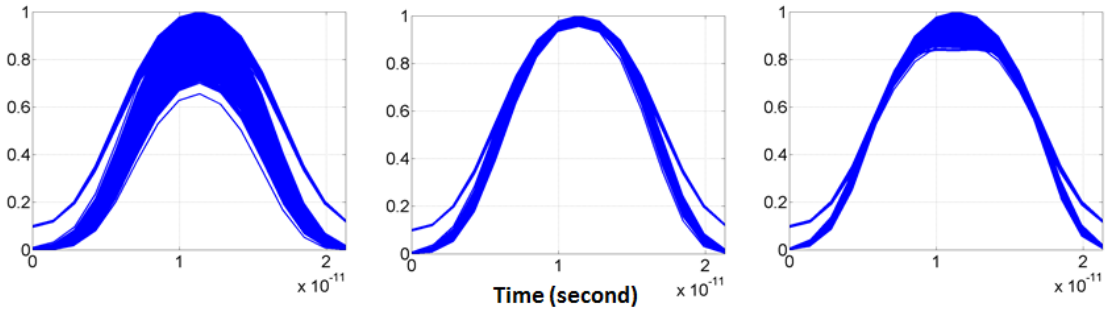

Figure 2.4. Transmitter eye diagram for transmission of 1024 pulses. From left to right, no pre-emphasis, case 3 pre-emphasis, and case 5 pre-emphasis. Optical power is normalized to unity peak power

As we wish to understand how the system performs under strong filtering, the eye diagram for the no pre-emphasis, case 3 and case 5 pre-emphases is reproduced following the optical BPF at the transmitter end for both the baseline and strong filtering cases. The two optical BPFs take on two 3 dB FWHM bandwidths at 75 GHz and 44.6 GHz for the baseline and strong filtering cases, respectively. In Figure 2.5, the baseline and strong optical filtering conditions yield divergent results for optimal eye performance. For weak optical filtering, the case 3 pre-emphasis produces the superior eye. However, for strong optical filtering, case 5 pre-emphasis produces the best eye clarity. With strong filtering, the transmitter-end optical BPF yields an NRZ-like signal shape as noted in Figure 2.5, consistent with the effect of a pulse-shaper.

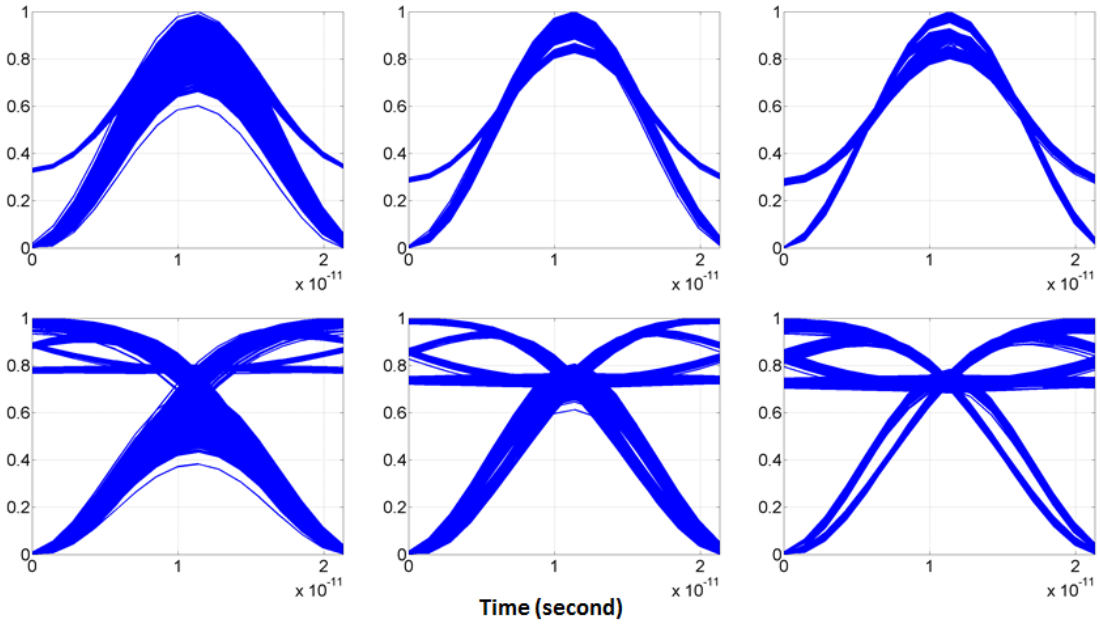

Figure 2.5. Eye diagram for pulse transmissions following the first optical BPF. The columns correspond to no pre-emphasis, case 3 and case 5 pre-emphases, respectively. The first row corresponds to weak optical filtering for 3dB bandwidth of 75 GHz, and the second row corresponds to strong optical filtering at 3 dB bandwidth of 44.6 GHz. The peak power is normalized to unity.

To more definitively examine the system performance, we follow the mathematical method prescribed in the previous subsection to provide BER performance. In this way, we are also able to examine the effect adjustments to our second PDPSK parameter, FSR. We first consider the BER without the inclusion of pre-emphasis. The BER is plotted against the 0.1 nm OSNR under both baseline and strong optical filtering conditions. As illustrated in Figure 2.6, FSR at 44 GHz yields the optimal performance across the series of FSR surveyed when overall optical filtering is at the baseline level. We note that the

associated delay between the two arms of the DLI is precisely T_b. For strong optical filtering, an FSR of 52 GHz elicits the best BER. In general, the overall BER performance over the range of FSR for baseline optical filtering is more favorable to that for strong optical filtering.

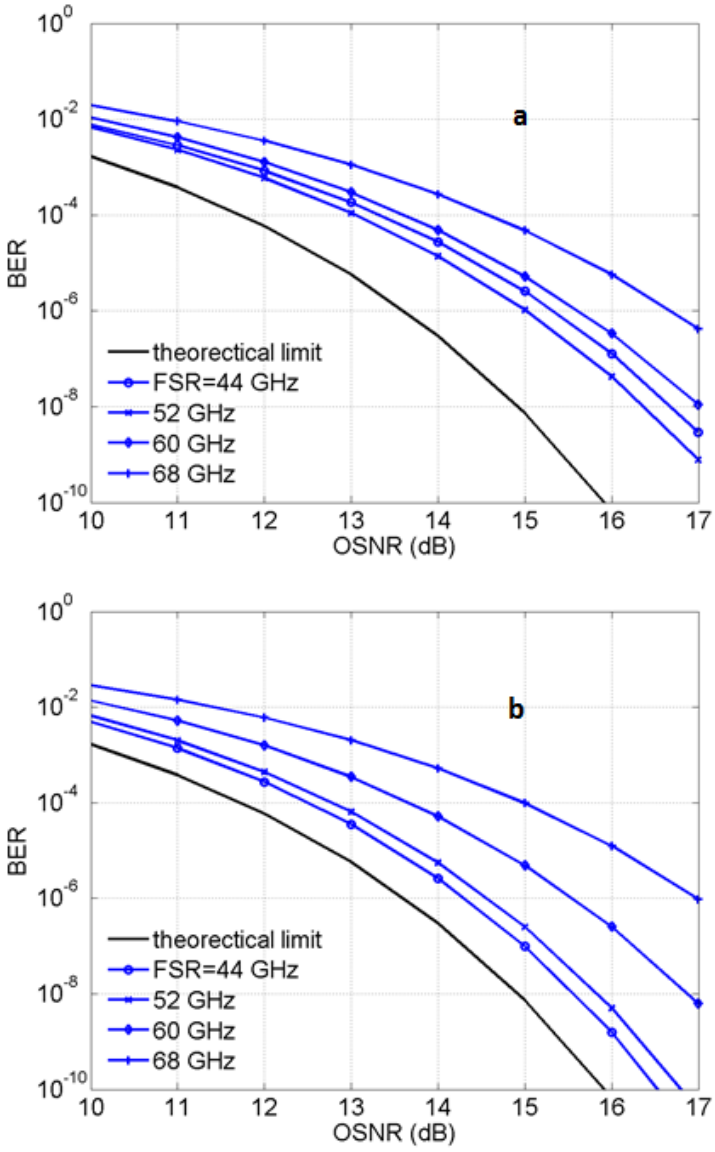

Figure 2.6. BER performance for 0.1 nm OSNR across 44 to 68 GHz with 4 GHz increments precluding pre-emphasis for strong (3 dB bandwidth 37.5 GHz) and baseline

(63.0 GHz) optical filtering, respectively. The theoretical limit to DPSK performance is included as a comparison

Next, we give consideration to the OSNR penalty across BER levels of 1e-3, 1e-4 and 1e-5. To do so, the value at each BER level for all FSR studied in the above Figure 2.6 is compared for baseline and strong optical filtering. The OSNR penalty is predicated upon the OSNR to provide the performance at each BER level. This comparison is shown in Figure 2.7, where we note that the best system performance occurs with DLI delay of T_b or 1-bit period for baseline optical filtering or FSR of 44 GHz. For the strong inline optical filtering case, the 48 GHz FSR results in the least OSNR penalty. Figure 2.7 provides a comprehensive comparison of the OSNR penalty for all pre-emphasis levels across all FSR bandwidths.

From Figure 2.7, it may be noted that the best performance may be achieved with a DLI tuned to a 1-bit period delay. However, the performance enhancements associated with increasing levels of pre-emphasis are negligible with exception at a higher BER level, 1e-5. For strong optical filtering, pre-emphasis achieves greater returns. As evident in Figure 2.7, at high BER = 1e-5, case 4 pre-emphasis reduces OSNR penalty by 0.3 dB.

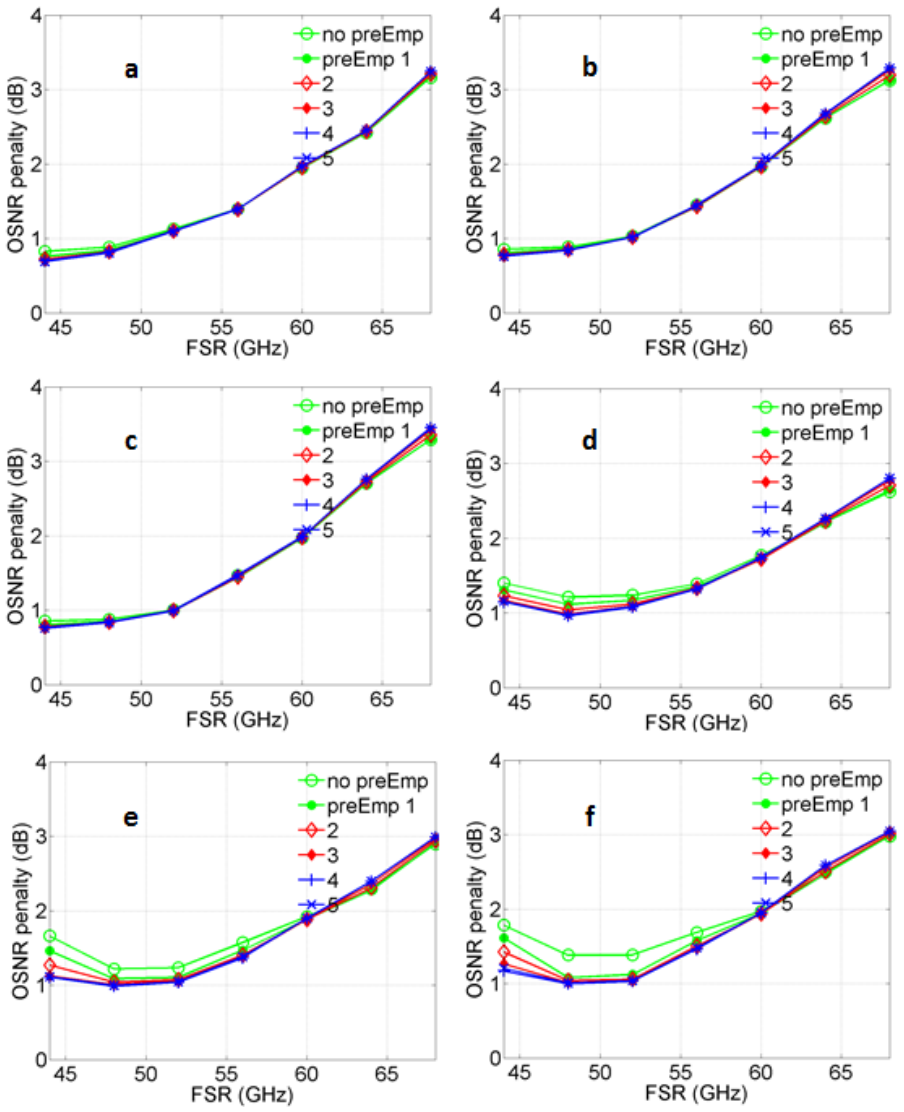

Figure 2.7. Panels a, b and c show OSNR penalty corresponding to FSR for varying pre-emphasis levels for baseline optical filtering (63 GHz) for BER = 1e-3, 1e-4, 1e-5, respectively. Panels d, e and f illustrate the same for strong optical filtering (37.5 GHz).

Thus, with the NZ-PDPSK transceiver model, the effect of pre-emphasis may be characterized as boosting system performance for strong optical filtering. With a wide inline optical filtering bandwidth, the effect of pre-emphasis is insignificant. Regarding FSR, an FSR slightly higher than the signal bit rate (48 GHz FSR as compared to 44 GHz

bit rate) for a narrow inline filtering bandwidth corresponding to strong optical filtering produces better system performance. As compared to the standard RZ-DPSK scheme where the FSR is not adjusted from the signal bit rate, RZ-PDPSK allows for improved OSNR performance exceeding 0.5 dB. Thus, we are able to conclude that the added flexibility of a tunable DLI can lead to improved performance in the case of strong optical filtering.

2.3 CONCLUSIONS

In our study of the RZ-PDPSK transceiver model, an objective comparison of the BER performance for all 4-bit patterns (using the De Bruijn sequence) is formed. Using pre-emphasis within the electrical signal driving path, the transceiver model is simulated with weak and strong optical filtering. Interestingly, strong optical filtering results in an NRZ waveform appearance. Under weak optical filtering conditions, pre-emphasis exacted minor improvement to OSNR performance. Furthermore, FSR equal to the bit rate offered the best performance. Under strong optical filtering, complementary pre-emphasis and FSR fine-tuning can yield up to 0.5 dB of OSNR improvement over RZ-DPSK transceivers without pre-emphasis for low BER = 1e-3.

Chapter 3

Constant Modulus Algorithm and Implementation with Dual Polarization Quadrature Phase-Shift Keying

3.1 Dual-Polarization Quadrature Phase-Shift Keying Systems

As mentioned in the introduction, the paradigm shift from purely intensity modulated OOK-based transceivers to phase modulation formats with coherent detection is motivated by the desire to enhance/maintain receiver sensitivity as well as improving bandwidth efficiency. Binary differential phase-shift keying (DPSK) has been demonstrated to increase receiver sensitivity correlating to > 1 dB savings at BER = 1e-3 in comparison to IM-DD systems. Coherent BPSK schemes yield 3 dB OSNR savings when compared to OOK at all BER, and coherent DPSK detection offers 2.2 dB OSNR savings compared to OOK at low BER = 1e-3 [16]. However, DPSK systems do not present any spectral efficiency improvements over OOK systems. Thus, coherent systems have garnered substantial attention due to the commonality of π-phase shifts shared with DPSK systems but the two factor compression of the spectrum as compared to DPSK schemes [8].

The phase modulation for coherent QPSK systems is brought about in the same fashion as that for DPSK. An MZM is used as a phase modulator, splitting light of equal from a

laser source into the two waveguides of the MZM. In one path, an optical π/2-phase shift occurs, producing one of four phases at the output of the MZM. The compressed spectrum of the QPSK format allows WDM systems to achieve high spectral efficiency for greater resistance to CD. In addition, the lengthier symbol duration allows DP-QPSK transceivers to resist PMD to a greater degree. Conversely, the compressed spectrum has its limitations as well. On the receiver end, the delay between the two branches within the DLI must be equivalent to the symbol duration, or twice the bit duration. Effectively, the receiver is six-times less tolerant to frequency drifts between transmitter and input to the DLI [6].

Nonetheless, with improved DSP on the receiver end, polarization-division multiplexing (PDM), the simultaneous transmission of two orthogonal polarizations at half the original signal bit rate, is possible even with the change in the state of polarization (SOP) across the fiber channel. If the two states remain nearly orthogonal across the entire channel with proper corrections to counteract PMD and depolarization attributed to fiber nonlinearity, coherent detection employed at the receiver end can effectively separate the two PDM channels with the correct DSP implemented. This joint employment of PDM and QPSK improves the spectral efficiency fourfold with respect to IM-DD schemes.

With pure phase encoding, it is desirable for the peak power to remain at a steady level. However, with the NRZ format, the average power input into each channel is drastically increased as a result of the symbol occupying the entire symbol duration. Moreover,

PMD and fiber nonlinearity prompt power invariability during signal transmission. Both of these issues may be lessened by using the RZ format in the DP-QPSK transceiver.

The true complexities of the DP-QPSK scheme lie in the demodulation of the transmitted signal. With pure phase-encoding, demodulation by means of direct detection is not possible due to the loss of all phase information in the detection process. For coherent schemes, two methods of detection exist, homodyne and heterodyne detection. Homodyne detection utilizes a local oscillator (LO) at the receiver end with a frequency precisely matching that of the carrier frequency. However, in practice, this is difficult due to the optical phase-locked loop that must be employed. Heterodyne detection methods have been more commonplace in microwave communications systems [17]. With the improvements to receiver end DSP, we examine the use of homodyne detection with a phase-diversity coherent receiver to effectively separate an incoming signal with an entirely arbitrary SOP [18].

Specifically, we are interested in polarization demultiplexing by means of SOP recovery using a two-by-two matrix representation to ascertain the change to the original SOP by means of adaptive filtering. We implement the constant-modulus algorithm (CMA) within the adaptive filtering scheme to control the recovery matrix [18]. In our coherent, RZ DP-QPSK scheme transceiver model, we are primarily interested in counteracting the change in SOP attributed to PMD. First, we describe the difficulties posed by PMD and then examine the mathematical underpinnings of the CMA.

3.2 Polarization-Mode Dispersion

As optical fiber systems are increasingly ubiquitous in long-haul applications, we must recognize and compensate for differing sources of channel effects and implement these corrections within transceiver realizations. Signal degradation attributed to PMD is of serious concern due to the random variations to the two orthogonal modes of polarization in a fiber.

At the source of PMD is optical birefringence. In an ideal, perfectly symmetrical fiber, two orthogonally polarized and degenerative HE_{11} modes exist with identical group delay. While fibers may be classified as single-mode fibers (SMF), two orthogonally polarized modes exist in all fibers. In practice, some degree of asymmetry is present due to manufacturing imperfections (intrinsic) or mechanical stresses enacted upon the fiber post-manufacture (extrinsic). When we examine a short fiber segment, we consider the birefringence to be uniform and linear with a determinable difference in propagation constants.

$$\Delta\beta = \frac{\omega n_s}{c} - \frac{\omega n_f}{c} = \frac{\omega \Delta n}{c}$$

where ω is the optical angular frequency, c is the speed of light, n_s and n_f are the effective refractive indices of the slow and fast modes, respectively, and Δn is the differential effective refractive index between the modes. The above expression is relevant to linear birefringence where two linear polarizations of waveguide modes exist in alignment with the symmetry of the fiber axes.

With the differential index Δn, the beat length, the distance over which a 2π phase difference between the two modes is incurred, may be defined as follows

$$L_b = \frac{\lambda}{\Delta n}$$

where λ is the optical wavelength. Effectively, the beat length represents a rotation of the polarization through a full cycle. To characterize the delay between the slow and fast modes or differential group delay (DGD), $\Delta\tau$, we determine the frequency derivative of the propagation constants as shown the following expression

$$\frac{\Delta\tau}{L} = \frac{d}{d\omega}\left(\frac{\Delta n\omega}{c}\right) = \frac{\Delta n}{c} + \frac{\omega}{c}\frac{d\Delta n}{d\omega}$$

The resulting short-length (intrinsic) PMD is thus expressed as $\Delta\tau/L$ in picoseconds per kilometer of fiber.

Over lengthy transmission distances of hundreds of thousands of kilometers, the deterministic property of DGD is no longer applicable. Rather than a single linear DGD, the birefringence axes vary randomly across the entire fiber span. The result is polarization-mode coupling, where the fast and slow modes decompose in to the fast and slow modes of each consecutive segment. At a large length, the power averages of the *x* and *y* polarizations $\langle p_x \rangle$ and $\langle p_y \rangle$ will converge do to polarization-mode coupling. For example, if $\langle p_x \rangle = 1$ and $\langle p_y \rangle = 0$ are input into a fiber, the difference between the two values will reach 0 across a very long span. In a long-length fiber, the correlation length L_c is the distance at which $\langle p_x \rangle - \langle p_y \rangle = 1/e^2$. As we can see, it is critical to mitigate this signal degradation and properly distinguish the two modes at the receiving end of the fiber.

3.3 CONSTANT MODULUS ALGORITHM

We are concerned with the concerned with optical signal demodulation in a homodyne receiver. The information signal is QPSK in binary representation with two bits per symbol and transmitted in a single state of polarization (SOP) at the transmitter. In QPSK modulation, each symbol of the information signal is expressed in four encoded phases, 00 = 45, 10 = 135, 11 = 225, and 01 = 315. The coherent nature of the homodyne receiver utilizes a local oscillator (LO) to drive signal modulation. We assume the LO signal frequency to match that of the carrier frequency and the timing is perfect.

The two relevant signals in this model include the information signal, E_s(t), at the transmitter expressed in eq. [3.1] with complex envelope, A_s(t), and carrier frequency component, $e^{j\omega_c t}$, and LO signal, E_{lo}(t), at the receiver expressed in eq. [3.2] with complex envelope, A_{lo}(t), and LO frequency component, $e^{j\omega_{lo} t}$. In our notation, subscript 's' corresponds to the general signal, 'sig' to information signal, 'c' to carrier, and 'lo' to local oscillator. The complex representation of both signals is shown below.

$$E_s(t) = A_s(t)e^{j\omega_c t} \quad [3.1]$$

$$E_{lo}(t) = A_{lo}(t)e^{j\omega_{lo} t} \quad [3.2]$$

The complex envelop of the complex representation of each signal is expressed in the following eqs. [3.3] and [3.4]

$$A_s(t) = \sqrt{P_s(t)}e^{j\theta_s(t)} = \sqrt{P_s(t)}e^{j[\theta_{sig}(t)+\phi_c(t)]} \quad [3.3]$$

$$A_{lo}(t) = \sqrt{P_{lo}(t)}e^{j\phi_{lo}(t)} \quad [3.4]$$

where the root of P_s(t) is the amplitude and θ_s(t) is the received signal phase, consisting of the transmitted signal phase θ_{sig}(t) and carrier phase noise component, ϕ_c(t). By employing the encoding rule, we may express the signal complex envelope as a pulse train, representing the signal as the sum of all symbols as shown in the following eq. [3.5]

$$A_s(t) = \sum_{k=0}^{\infty} \sqrt{P_s\left(t - kT_{\text{sym}}\right)} e^{j\left\{[2(i_1)_k + (i_0)_k]\frac{2\pi}{4} + \frac{2\pi}{8} + \phi_c(t)\right\}} \qquad [3.5]$$

where the product of amplitude across the kth symbol period, T_{sym}, is multiplied by the exponential containing the encoding rule expression.

Following signal propagation, the information signal, E_s, is composed of two SOPs due to transmittance effects as shown in eq. [3.6] below. The LO, expressed in two SOP in eq. [3.7], is evenly divided between both H- and V-data lanes since the signal is a controlled entity in coherent detection.

$$\begin{bmatrix} E_{sH}(t) \\ E_{sV}(t) \end{bmatrix} = \begin{bmatrix} \sqrt{\alpha} A_s(t) e^{j\delta} \\ \sqrt{1-\alpha} A_s(t) \end{bmatrix} e^{j\omega_c t} \qquad [3.6]$$

$$\begin{bmatrix} E_{loH}(t) \\ E_{loV}(t) \end{bmatrix} = \frac{1}{\sqrt{2}} \begin{bmatrix} A_{lo}(t) \\ A_{lo}(t) \end{bmatrix} e^{j\omega_{lo} t} \qquad [3.7]$$

However, the uncertainty of the modulated signal SOP requires splitting the dividing the complex envelop into two components with a ratio α and phase difference δ to differentiate between H and V components. In order to derive the original signal from the modulated signal, we must first ascertain the value of α and δ. We begin by expressing the resultant electric fields generated by the 90° optical hybrid. Eight different electric field components are generated for both the modulated and LO signals.

$$\begin{bmatrix} E_1 \\ E_2 \\ E_3 \\ E_4 \end{bmatrix} = \frac{1}{2}\begin{bmatrix} 1 & 1 \\ 1 & -1 \\ 1 & j \\ 1 & -j \end{bmatrix}\begin{bmatrix} E_{sH} \\ E_{loH} \end{bmatrix}$$

$$\begin{bmatrix} E_5 \\ E_6 \\ E_7 \\ E_8 \end{bmatrix} = \frac{1}{2}\begin{bmatrix} 1 & 1 \\ 1 & -1 \\ 1 & j \\ 1 & -j \end{bmatrix}\begin{bmatrix} E_{sV} \\ E_{loV} \end{bmatrix}$$

The electric field acting upon the photodiodes following the 90° optical hybrid results in the generation of four total photocurrents for both the *H* and *V* components. We name these currents $I_{PD1\ldots4}$. We will illustrate the derivation for photocurrent I_{PD1} below, recalling the assumption of carrier and LO frequency equality ($\omega_c = \omega_{lo}$)

$$\begin{aligned} I_{PD1} &= R[|E_1|^2 - |E_2|^2] \\ &= R\frac{1}{4}[(E_{sH} + E_{loH})(E_{sH} + E_{loH})^* - (E_{sH} - E_{loH})(E_{sH} - E_{loH})^*] \\ &= R\frac{1}{4}[2{E_{sH}}^* E_{loH} + 2E_{sH}{E_{loH}}^*] \\ &= R\frac{1}{2}\sqrt{\frac{\alpha}{2}}\left[{A_{sH}}^* e^{-j\delta}e^{-j\omega_c t}A_{loH}e^{j\omega_{lo}t} + A_{sH}e^{j\delta}e^{j\omega_c t}{A_{loH}}^* e^{-j\omega_{lo}t}\right] \\ &= R\sqrt{\frac{\alpha P_s(t)P_{lo}(t)}{2}}\left[\frac{e^{-j[\theta_s(t)+\phi_c(t)+\delta]}e^{j\phi_{lo}(t)} + e^{j[\theta_s(t)+\phi_c(t)+\delta]}e^{-j\phi_{lo}(t)}}{2}\right] \\ &= R\sqrt{\frac{\alpha P_s(t)P_{lo}(t)}{2}}\cos[\theta_s(t) + \phi_c(t) - \phi_{lo}(t) + \delta] \end{aligned}$$

Doing the same for the remaining photocurrents, $I_{PD1\ldots4}$ are expressed as follows

$$I_{PD1} = R\sqrt{\frac{\alpha P_s(t)P_{lo}(t)}{2}}\cos[\theta_s(t) + \phi_c(t) - \phi_{lo}(t) + \delta]$$

$$I_{PD2} = R\sqrt{\frac{\alpha P_s(t)P_{lo}(t)}{2}}\sin[\theta_s(t) + \phi_c(t) - \phi_{lo}(t) + \delta]$$

$$I_{PD3} = R\sqrt{\frac{(1-\alpha)P_s(t)P_{lo}(t)}{2}}\cos[\theta_s(t) + \phi_c(t) - \phi_{lo}(t)]$$

$$I_{PD4} = R\sqrt{\frac{(1-\alpha)P_s(t)P_{lo}(t)}{2}}\sin[\theta_s(t) + \phi_c(t) - \phi_{lo}(t)]$$

where the known value R is the responsivity, or the ratio of generated photocurrent to light power. While the value for the photocurrents is known, the information signal, θ_{sig}(t) must be determined. In order to solve for θ_{sig}(t), the parameters α and δ as well as carrier and local oscillator phase noise must be established first. We may first solve for δ by combining the expressions for photocurrents 1, 2 and 3, 4 to yield two tangent expressions.

$$\frac{I_{PD2}}{I_{PD1}} = \tan[\theta_s(t) + \phi_c(t) - \phi_{lo}(t) + \delta]$$

$$\frac{I_{PD4}}{I_{PD3}} = \tan[\theta_s(t) + \phi_c(t) - \phi_{lo}(t)]$$

From the above ratios, δ may be determined by simple trigonometric manipulation. With the known value of δ, we may determine the value of α by combining the expressions for photocurrents 1 and 3 as shown below

$$\frac{I_{PD3}}{I_{PD1}} = \sqrt{\frac{1-\alpha}{\alpha}}e^{-j\delta}$$

Further algebraic manipulation will yield α. Lastly, the carrier and LO phase noise must be established to return the information signal. Having ascertained values for α and δ, we may apply the Viterbi algorithm to eliminate θ_{sig}(t) from the photocurrent expression to find phase noise. In QPSK modulation, raising the photocurrent to the fourth power will

eliminate θ_{sig}(t) due to the quadrature nature of the information signal. We demonstrate in the following algebraic manipulation

$$I_{PD3}{}^4 = R^4 \left[\frac{(1-\alpha)P_s(t)P_{lo}(t)}{2}\right]^2 e^{4j[\theta_s(t)+\phi_c(t)-\phi_{lo}(t)]}$$

$$I_{PD3}{}^4 = R^4 \left[\frac{(1-\alpha)P_s(t)P_{lo}(t)}{2}\right]^2 e^{4j[\phi_c(t)-\phi_{lo}(t)]}$$

The second expression may be manipulated to determine the amount of phase noise from both carrier and LO, $\phi_c(t) - \phi_{lo}(t)$, since all other values in the expression are known. Thus, with all parameters known, we may substitute all known values and to attain the demodulated information signal θ_{sig}(t).

3.4 KIKUCHI SETUP DERIVATION

The Kikuchi setup models a polarization demux circuit with the signal complex envelop expressed in two polarization states *x* and *y* [18] shown in Figure 3.1. Upon entering the receiver, these two SOP are equally split into two branches to produce two SOP, E_x and E_y, with arbitrary mixing of the original SOPs in each branch. Following the adaptive filtering recovery of the original SOP with the two-by-two corrective matrix alluded to previously, two SOP are produced, E_X and E_Y, that match the original transmitted signals, $E_{in,x}$ and $E_{in,y}$. However, the recovery of the original SOP does not necessarily match $E_{in,x}$ with E_X. Rather, the recovered SOP could yield $E_Y = E_{in,x}$ or vice versa. From this point on, we will term the complex envelope of the signal with $E_j = A_j$ where $j = \{x, y\}$.

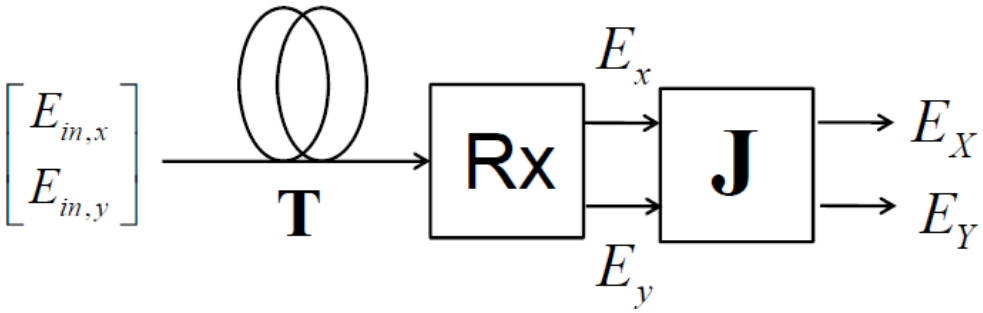

Figure 3.1. Kikuchi setup with channel effects described by two-by-two, unitary matrix ***T*** and recovery matrix ***J*** [29]

During transmission, the transmission effects are represented by unitary matrix ***T***, yielding the following expression

$$\begin{bmatrix} A_x(t) \\ A_y(t) \end{bmatrix} = T \begin{bmatrix} A_{in,x}(t) \\ A_{in,y}(t) \end{bmatrix} = \begin{bmatrix} \sqrt{\alpha}e^{j\delta} & -\sqrt{1-\alpha} \\ \sqrt{1-\alpha} & \sqrt{\alpha}e^{-j\delta} \end{bmatrix} \begin{bmatrix} A_{in,x}(t) \\ A_{in,y}(t) \end{bmatrix}$$

Modifying the Kikuchi notation, we express the phase difference between *x* and *y* confined to input *x*. This is a sensible modification since it would be sensible for a single input to be phase delayed from the other rather than a phase-delayed component for each signal. This expression is shown below.

$$\begin{bmatrix} A_x(t) \\ A_y(t) \end{bmatrix} = T \begin{bmatrix} A_{in,x}(t) \\ A_{in,y}(t) \end{bmatrix} = \begin{bmatrix} \sqrt{\alpha}e^{j\delta} & -\sqrt{1-\alpha}e^{j\delta} \\ \sqrt{1-\alpha} & \sqrt{\alpha} \end{bmatrix} \begin{bmatrix} A_{in,x}(t) \\ A_{in,y}(t) \end{bmatrix}$$

Another realization of the Kikuchi notation is centering the signal peaks around $f = 0$, with one signal peak located at $\delta/2$ and the other at $-\delta/2$. This expression is expressed below

$$\begin{bmatrix} A_x(t) \\ A_y(t) \end{bmatrix} = T \begin{bmatrix} A_{in,x}(t) \\ A_{in,y}(t) \end{bmatrix} = \begin{bmatrix} \sqrt{\alpha}e^{j\delta/2} & -\sqrt{1-\alpha}e^{j\delta/2} \\ \sqrt{1-\alpha}e^{-j\delta/2} & \sqrt{\alpha}e^{-j\delta/2} \end{bmatrix} \begin{bmatrix} A_{in,x}(t) \\ A_{in,y}(t) \end{bmatrix}$$

It is important to note that the above three interpretations are equivalent in accordance to the steady-state convergence criteria of the polarization demux model and may be confirmed as such mathematically.

The complex representation of the information signal is shown below, also expressed with the unitary transmittance matrix.

$$\begin{bmatrix} E_{sH1}(t) \\ E_{sV1}(t) \end{bmatrix} = \begin{bmatrix} e^{j\delta/2} & 0 \\ 0 & e^{-j\delta/2} \end{bmatrix} \begin{bmatrix} \cos\theta & -\sin\theta \\ \sin\theta & \cos\theta \end{bmatrix} \begin{bmatrix} A_{in,x} \\ A_{in,y} \end{bmatrix}$$

$$= \begin{bmatrix} \cos\theta\, e^{j\delta/2} & -\sin\theta\, e^{j\delta/2} \\ \sin\theta\, e^{-j\delta/2} & \cos\theta\, e^{-j\delta/2} \end{bmatrix} \begin{bmatrix} A_{in,x} \\ A_{in,y} \end{bmatrix}$$

However, we are concerned with the transmission effects upon the complex envelop and will continue to develop the algorithm to determine the correction matrix ***J***. Since we assume the transmission effects can be represented by unitary matrix ***T***, we also assume ***J*** to be unitary as well.

$$\mathbf{J} = \begin{bmatrix} r & k \\ -k^* & r^* \end{bmatrix}$$

As such, we define matrix ***C*** as the matrix product of ***J*** and ***T*** with matrix components as expressed below

$$C_{11} = r\sqrt{\alpha}e^{j\delta} + k\sqrt{1-\alpha}$$

$$C_{12} = -r\sqrt{1-\alpha}e^{j\delta} + k\sqrt{\alpha}$$

$$C_{21} = -k^*\sqrt{\alpha}e^{j\delta} + r^*\sqrt{1-\alpha} = -{C_{12}}^*$$

$$C_{22} = k^*\sqrt{1-\alpha}e^{j\delta} + r^*\sqrt{\alpha} = {C_{11}}^*$$

Therefore, the expression with matrix ***C*** is as follows

$$\begin{bmatrix} A_H(t) \\ A_V(t) \end{bmatrix} = \mathbf{C} \begin{bmatrix} A_{in,x}(t) \\ A_{in,y}(t) \end{bmatrix} = \begin{bmatrix} C_{11} & C_{12} \\ C_{21} & C_{22} \end{bmatrix} \begin{bmatrix} A_{in,x}(t) \\ A_{in,y}(t) \end{bmatrix}$$

We must recognize that to fulfill the function of the polarization demux, the value of $\boldsymbol{C}$ will allow for two scenarios

$$\begin{bmatrix} A_H(t) \\ A_V(t) \end{bmatrix} \propto \begin{bmatrix} A_{in,x}(t) \\ A_{in,y}(t) \end{bmatrix} \text{or} \quad \begin{bmatrix} A_H(t) \\ A_V(t) \end{bmatrix} \propto \begin{bmatrix} A_{in,y}(t) \\ A_{in,x}(t) \end{bmatrix}$$

$\boldsymbol{C}$ must also be a unitary matrix, enabling the determination of both $A_H(t)$ and $A_V(t)$ by solving for one data lane or the other. As required by the polarization demux, either C_{12} (case 1) or C_{11} (case 2) must be 0 as we see in the following relationship

$$A_H(t) = C_{11}A_{in,x}(t) + C_{12}A_{in,y}(t)$$

If $|A_H(t)|^2$ or $|A_V(t)|^2 = 1$, then $|A_H(t)|^2$ = constant. This may be expressed as the following

$$|A_H(t)|^2 = \left|C_{11}A_{in,x}(t)\right|^2 + \left|C_{12}A_{in,y}(t)\right|^2 + 2\left|C_{11}A_{in,x}(t)C_{12}A_{in,y}(t)\right| \cos\vartheta = \text{const.}$$

where the time variance term (third term) must be 0. Only without the third term may the polarization demux requirement for the occurrence of either case 1 or case 2 be realized. Effectively, CMA will yield $\boldsymbol{J}$ where $|A_H(t)|^2$ is a constant. To reiterate, we present both cases below.

Case 1 is satisfied when

$$C_{12} = -r\sqrt{1-\alpha}e^{j\delta} + k\sqrt{\alpha} = 0 \Rightarrow \frac{r}{k} = \frac{\sqrt{\alpha}}{\sqrt{1-\alpha}e^{j\delta}}$$

resulting in

$$A_H(t) = C_{11}A_{in,x}(t) = \frac{k}{\sqrt{1-\alpha}}A_{in,x}(t)$$

To normalize $|A_H(t)|^2 = 1$, $k = \sqrt{1-\alpha}e^{j\xi}$ and it follows that $r = \sqrt{\alpha}e^{-j\delta+j\xi}$. Thus, we establish A_H and A_V to be

$$A_H(t) = \frac{k}{\sqrt{1-\alpha}} A_{in,x}(t) = A_{in,x}(t)e^{j\xi}$$

$$A_V(t) = A_{in,y}(t)e^{-j\xi}$$

Due to the unitary nature of the matrices, we note that the value of A_H and A_V are simultaneously established where $C_{11} = e^{j\xi}$.

Case 2 is similar, with $r = \sqrt{1-\alpha}e^{j\zeta}$ and $k = \sqrt{\alpha}e^{j\delta+j\zeta}$

$$A_H(t) = A_{in,y}(t)e^{j\zeta}$$

$$A_V(t) = -A_{in,x}(t)e^{-j\zeta}$$

where $C_{12} = e^{j\zeta}$.

In order to determine the correction matrix ***J***, we begin with a set of initial values corresponding to matrix ***P*** as follows

$$\begin{bmatrix} A_H[0] \\ A_V[0] \end{bmatrix} = \mathbf{P}[0] \begin{bmatrix} A_x[n] \\ A_y[n] \end{bmatrix} = \begin{bmatrix} \tilde{r}[0] & \tilde{k}[0] \\ -\tilde{k}[0]^* & \tilde{r}[0]^* \end{bmatrix} \begin{bmatrix} A_x[n] \\ A_y[n] \end{bmatrix}$$

Applying the statistical gradient method, the following iterative formula is formed

$$\tilde{r}[n+1] = \tilde{r}[n] + \mu(1 - |A_H[n]|^2)A_H[n]A_x[n]^*$$

$$\tilde{k}[n+1] = \tilde{k}[n] + \mu(1 - |A_H[n]|^2)A_H[n]A_y[n]^*$$

where μ is the step size and $(1 - |A_H(t)|^2)$ denotes error. With the convergence the first row of matrix ***P***, the entire DSP circuit will work, yielding A_V.

In the scenario where transmittance effects result in signal loss, characterizing the polarization dependent loss yields the following non-unitary matrix ***P***. In this situation, convergence of both the H- and V- data lanes is required to yield the demodulated signal.

$$\mathbf{P} = \begin{bmatrix} p_{xx} & p_{xy} \\ p_{yy} & p_{yx} \end{bmatrix}$$

with the corresponding iterative formula

$$p_{xx}[n+1] = p_{xx}[n] + \mu(1 - |A_H[n]|^2)A_H[n]A_x[n]^*$$

$$p_{xy}[n+1] = p_{xy}[n] + \mu(1 - |A_H[n]|^2)A_H[n]A_y[n]^*$$

$$p_{yy}[n+1] = p_{yy}[n] + \mu(1 - |A_H[n]|^2)A_V[n]A_x[n]^*$$

$$p_{yx}[n+1] = p_{yx}[n] + \mu(1 - |A_H[n]|^2)A_V[n]A_y[n]^*$$

The underlying DSP for characterization of PDL is better visualized in Figure 3.2 which reveals the progression of the received signal to recovery of the original SOP.

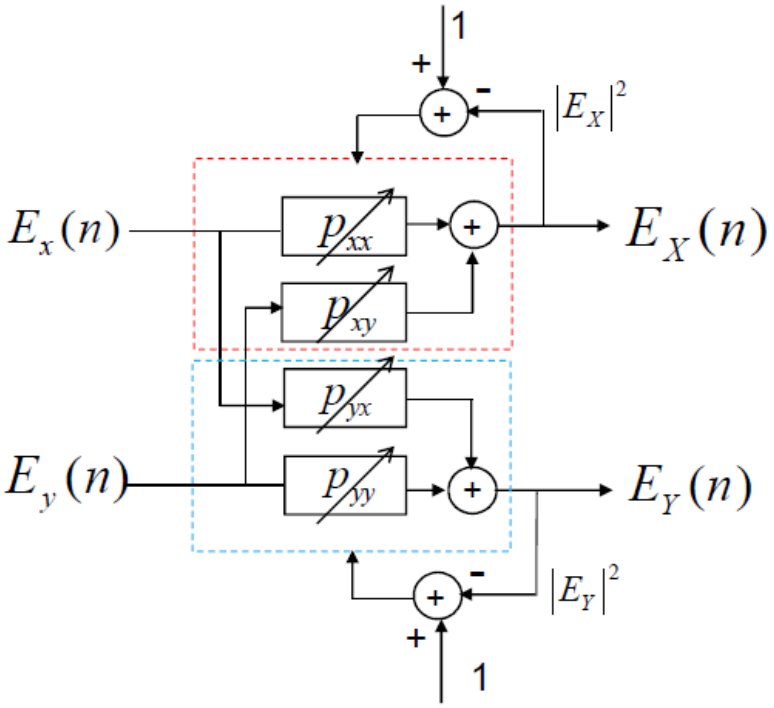

Figure 3.2. DSP circuit for control of state of polarization. Once again, A_j = Ej where j = $\{x, y\}$ [18]

Tranceiver imperfections result in intersymbol interference (e.g. insufficient bandwidth, residual CD, and PMD). We may merge CMA with feed-forward equalization (FFE) to enhance system functionality. In this model, 16 T/2 taps are employed. We illustrate an initial matrix ***P*** as shown below

$$\begin{bmatrix} A_{Hi}{}^{[0]}[n] + jA_{Hq}{}^{[0]}[n] \\ A_{Vi}{}^{[0]}[n] + jA_{Vq}{}^{[0]}[n] \end{bmatrix} = \sum_{k=0}^{N} \mathbf{P}^{[k]}[0] \begin{bmatrix} A_{xi}[n-k] + jA_{xq}[n-k] \\ A_{yi}[n-k] + jA_{yq}[n-k] \end{bmatrix}$$

$$\mathbf{P}^{k}[0] = \begin{bmatrix} \tilde{r}_i{}^{[0]}[k] + j\tilde{r}_q{}^{[0]}[k] & \tilde{k}_i{}^{[0]}[k] - j\tilde{k}_q{}^{[0]}[k] \\ -\tilde{k}_i{}^{[0]}[k] + j\tilde{k}_q{}^{[0]}[k] & \tilde{r}_i{}^{[0]}[k] - j\tilde{r}_q{}^{[0]}[k] \end{bmatrix}$$

To differentiate the real and imaginary modes, we rearrange the matrices in the following

$$\begin{bmatrix} A_{Hi}{}^{[0]}[n] \\ A_{Hq}{}^{[0]}[n] \\ A_{Vi}{}^{[0]}[n] \\ A_{Vq}{}^{[0]}[n] \end{bmatrix} = \sum_{k=0}^{N} \mathbf{P}_{\mathrm{R}}{}^{[k]}[0] \begin{bmatrix} A_{xi}{}^{[0]}[n-k] \\ A_{xq}{}^{[0]}[n-k] \\ A_{yi}{}^{[0]}[n-k] \\ A_{yq}{}^{[0]}[n-k] \end{bmatrix}$$

$$\mathbf{P}_{\mathrm{R}}{}^{[k]}[0] = \begin{bmatrix} \tilde{r}_i{}^{[0]}[k] & -\tilde{r}_q{}^{[0]}[k] & \tilde{k}_i{}^{[0]}[k] & -\tilde{k}_q{}^{[0]}[k] \\ \tilde{r}_q{}^{[0]}[k] & \tilde{r}_i{}^{[0]}[k] & \tilde{k}_q{}^{[0]}[k] & \tilde{k}_i{}^{[0]}[k] \\ -\tilde{k}_i{}^{[0]}[k] & -\tilde{k}_q{}^{[0]}[k] & \tilde{r}_i{}^{[0]}[k] & \tilde{r}_q{}^{[0]}[k] \\ \tilde{k}_q{}^{[0]}[k] & -\tilde{k}_i{}^{[0]}[k] & -\tilde{r}_q{}^{[0]}[k] & \tilde{r}_i{}^{[0]}[k] \end{bmatrix}$$

We first concern ourselves with the complex data and complex coefficients, modifying the iterative ***P*** matrix components to the following

$$\bar{p}_{xx}{}^{[I+1]} = \bar{p}_{xx}{}^{[I]} + \mu \left(1 - \left|A_H{}^{[I]}\right|^2\right) A_H{}^{[I]} \bar{A}_x{}^{[I]^*}$$

$$\bar{p}_{xy}{}^{[I+1]} = \bar{p}_{xy}{}^{[I]} + \mu \left(1 - \left|A_H{}^{[I]}\right|^2\right) A_H{}^{[I]} \bar{A}_y{}^{[I]^*}$$

$$\bar{p}_{yy}{}^{[0]} = \bar{p}_{xx}{}^{[\infty]^*}$$

$$\bar{p}_{yx}{}^{[0]} = -\bar{p}_{xy}{}^{[\infty]^*}$$

We represent the ***P*** matrix elements with $\tilde{r}$ and $\tilde{k}$, which are shown as follow

$$\bar{p}_{xx}{}^{[I]}[k] = \tilde{r}_i{}^{[I]}[k] + j\tilde{r}_q{}^{[I]}[k]$$

$$\bar{p}_{xy}{}^{[I]}[k] = \tilde{k}_i{}^{[I]}[k] + j\tilde{k}_q{}^{[I]}[k]$$

The addition of the over-bar indicates that these parameters are no longer scalar but 16x1 column vectors inclusive of all 16 taps of the CL4010. The above expressions indicate an initial input of A_H leading to an iterative progression to a steady state, converging upon either A_x and A_y.

$$\tilde{r}_i{}^{[I+1]}[k] = \tilde{r}_i{}^{[I]}[k] + \mu\left(1 - \left|A_H{}^{[I]}\right|^2\right)(A_{Hi}{}^{[I]}A_{xi}{}^{[I]}[k] + A_{Hq}{}^{[I]}A_{xq}{}^{[I]}[k])$$

$$\tilde{r}_q{}^{[I+1]}[k] = \tilde{r}_q{}^{[I]}[k] + \mu\left(1 - \left|A_H{}^{[I]}\right|^2\right)(-A_{Hi}{}^{[I]}A_{xq}{}^{[I]}[k] + A_{Hq}{}^{[I]}A_{xi}{}^{[I]}[k])$$

$$\tilde{k}_i{}^{[I+1]}[k] = \tilde{k}_i{}^{[I]}[k] + \mu\left(1 - \left|A_H{}^{[I]}\right|^2\right)(A_{Hi}{}^{[I]}A_{yi}{}^{[I]}[k] + A_{Hq}{}^{[I]}A_{yq}{}^{[I]}[k])$$

$$\tilde{k}_q{}^{[I+1]}[k] = \tilde{k}_q{}^{[I]}[k] + \mu\left(1 - \left|A_H{}^{[I]}\right|^2\right)(-A_{Hi}{}^{[I]}A_{yq}{}^{[I]}[k] + A_{Hq}{}^{[I]}A_{yi}{}^{[I]}[k])$$

In accordance to our first discussion of the ***P*** matrix, the V-data lane must be established as well since transmittance effects result in a non-unitary correction matrix where attaining a single data lane will allow the determination of the other data lane. As such, we reassign the *yx* and *yy* ***P*** matrix elements to the following

$$\bar{p}_{yx}{}^{[I+1]} = \bar{p}_{yx}{}^{[I]} + \mu\left(1 - \left|A_V{}^{[I]}\right|^2\right)A_V{}^{[I]}\bar{A}_x{}^{[I]^*}$$

$$\bar{p}_{yy}{}^{[I+1]} = \bar{p}_{yy}{}^{[I]} + \mu\left(1 - \left|A_V{}^{[I]}\right|^2\right)A_V{}^{[I]}\bar{A}_y{}^{[I]^*}$$

The resulting $\tilde{r}$ and $\tilde{k}$ iterative terms are then expressed as previously listed for the H-data lane, substituting for the *Hi* and *Hq* terms with *V* terms accordingly. In doing so, the original information signals may be found.

3.5 CMA-FFE TRANSCEIVER MODEL

In our simulation environment, a bit sequence is passed through a 5th order Bessel LPF to mimic non-ideal NRZ pulses. Inter-symbol interference is introduced to the non-ideal pulse, and the sequence is subsequently passed through a dispersive channel. CD is simulated across a 1000 km span with dispersion-associated delay of 4.096 ps/km. In Figure 3.3, we show the ideal, transmitted and CD-degraded pulse sequences.

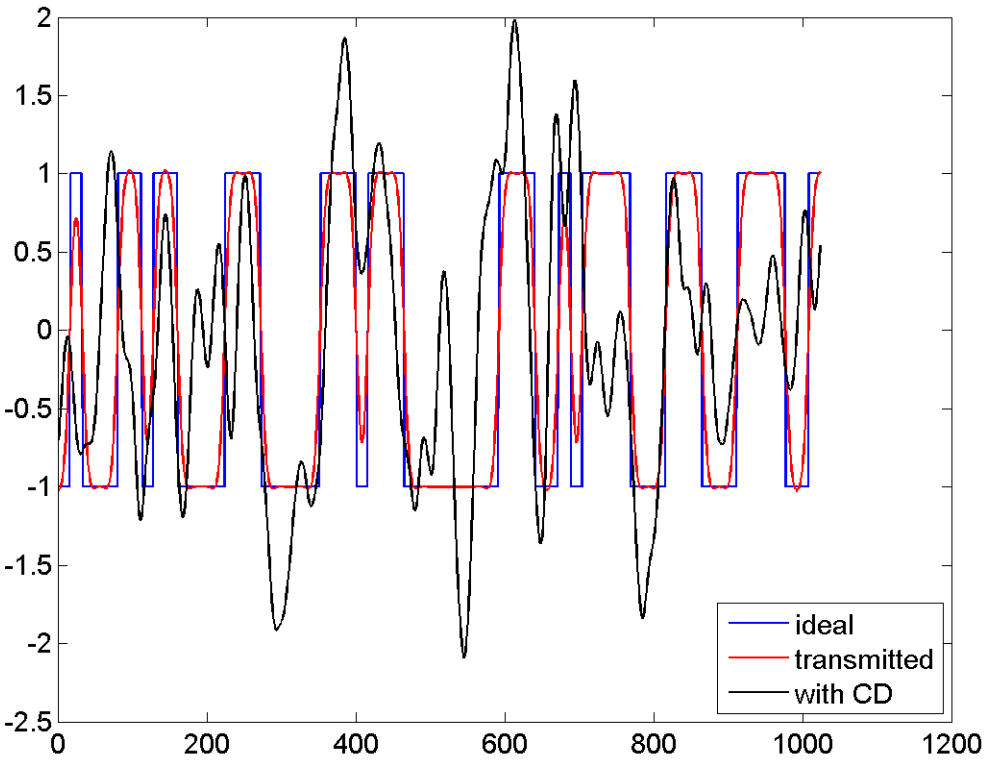

Figure 3.3. Idea, transmitted, and CD-degraded pulse sequences

In our first simulation environment setup, we merge CMA and FFE with variations to step-size μ = 1/64 and 1/1028 and number of taps T = 4. The CMA-FFE setup without

moving average is illustrated below in Figure 3.4, depicting the receiver signal progression for SOP recovery.

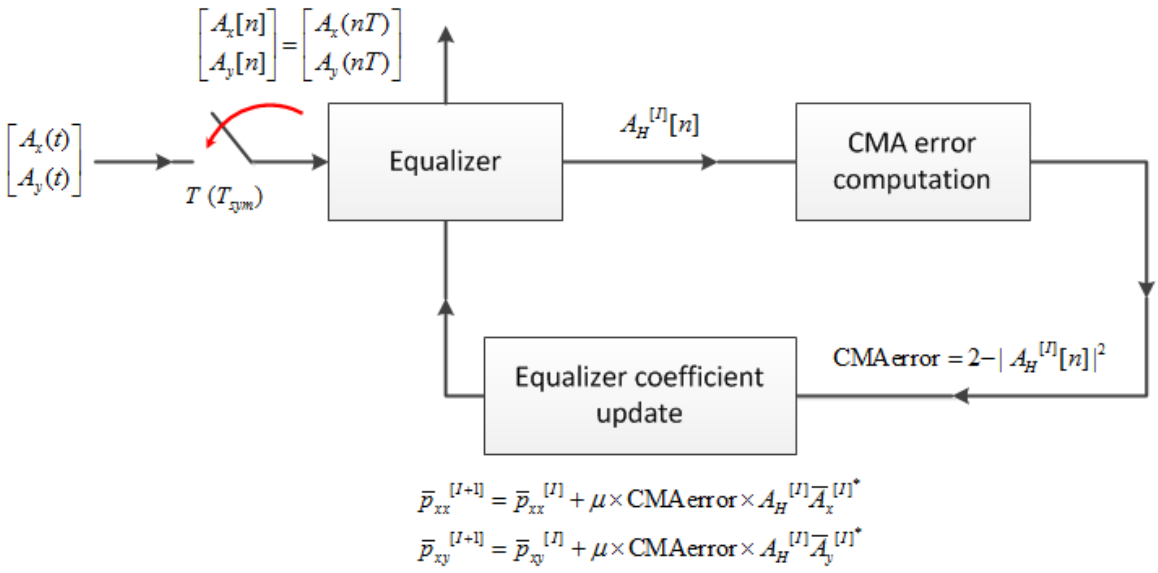

Figure 3.4. CMA-FFE without moving average

In Figure 3.5, the FFE is better detailed, indicating the tap coefficients and signal progression. The disadvantage of the CMA-FFE lacking a moving average during equalization is the consideration of forward information only. The filter is adapting to what bits have passed through the equalizer and the present bit.

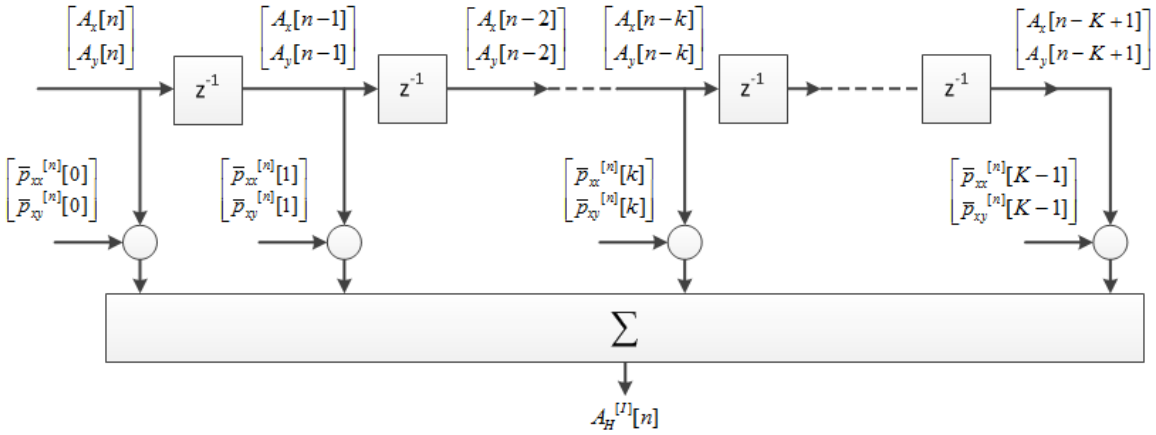

Figure 3.5. Feed-forward equalizer without moving average

3.6 SIMULATION RESULTS

For the CMA-FFE case without moving average, we visually inspect the constellation diagram for differing step sizes. To achieve a satisfactory BER, tradeoffs must always be made for acceptable BER at the cost of system performance. As such, we consider differing step sizes for the explicit purpose of determine a satisfactory constellation at the cost of slower tap convergence. In Figures 3.6 and 3.7, we consider a large step size μ = 1/64 and a smaller step size 1/1028.

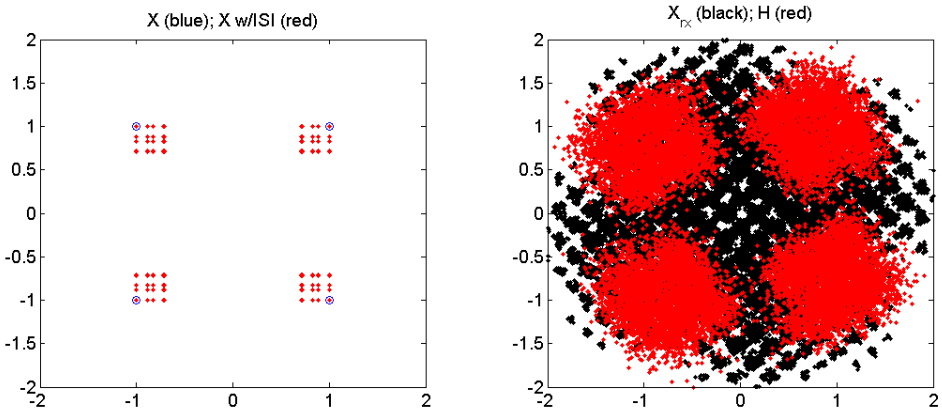

Figure 3.6. CMA-FFE without moving average, step size μ = 1/64. The left panel illustrates the ideal constellation for bits transmitted and the bits with ISI accumulated over the entirety of the channel. The right panel shows the constellation map of the signal upon arrival (black) at the receiver and following equalization (red)

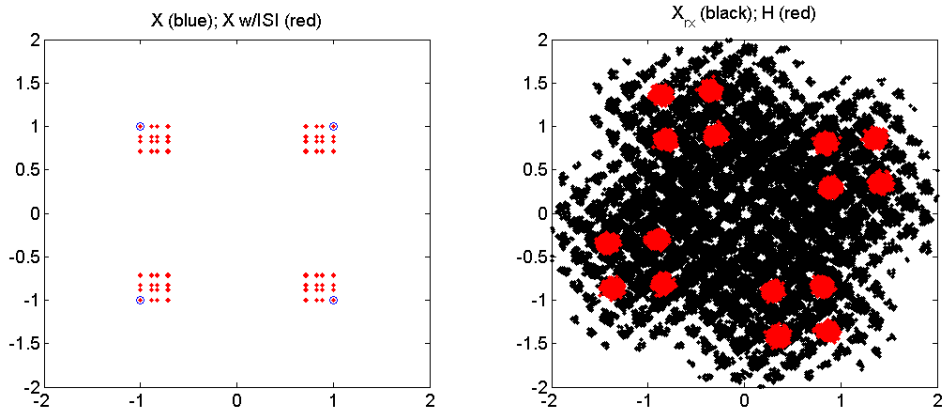

Figure 3.7. CMA-FFE without moving average, step size μ = 1/1028

It is readily apparent that the smaller step size yields a significant improvement to the equalization for recovery of the original SOP. To inspect the bit sequence recovery, a short bit sequence is shown in the following Figure 3.8 for the large and small step sizes.

As we can see from the bit sequences for the large and small step sizes, we note that the smaller step size does prove to be capable of restoring the signal amplitude in equalization for signal recovery. However, within a 20 bit sequence, we note that while the incorrect bits are closer to 0 amplitude in the setup with a smaller step size, 12 and 8 bit errors are present for the *i* and *q* channels for both step sizes. For a short sequence, this represents an unacceptable BER for overall system performance across the entire

signal. In practice, these bit errors can be readily corrected with additional DSPs immediately following equalization. Similar to the BPSK and DPSK comparison where DPSK implements differential encoding in order to prevent lengthy segments of cycle-slip, the cycle-slip that may surface in a QPSK scheme can be mitigated simply by the addition of an additional MZM stage for different QPSK encoding following carrier recovery. As such, a DP-QPSK setup can be converted to a DP-DQPSK setup with the addition of an additional MZM stage prior to transmission and immediately after decoding.

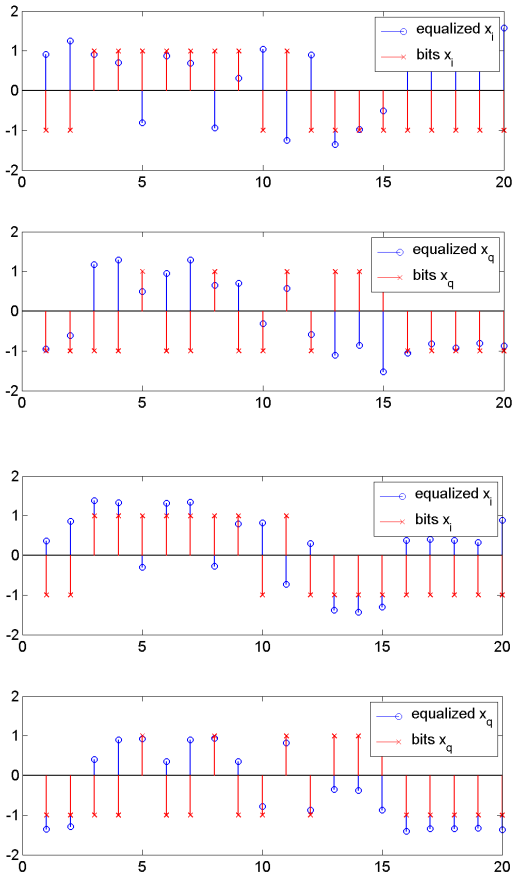

Figure 3.8. CMA-FFE without moving average, step size μ = 1/64, 1/1028 for the left and right panels, respectively. The upper and lower rows show the recovery of the channel polarizations *i* and *q*

Another aspect we may also evaluate is the rate at which the equalizer will attain tap convergence upon an acceptable set of tap coefficients. For the CMA-FFE case without moving average, we can visually evaluate the number of iterations required to achieve tap convergence. Ideally, the equalizer will converge to set of accurate tap coefficients quickly in order to reduce the number of errors output from the receiver.

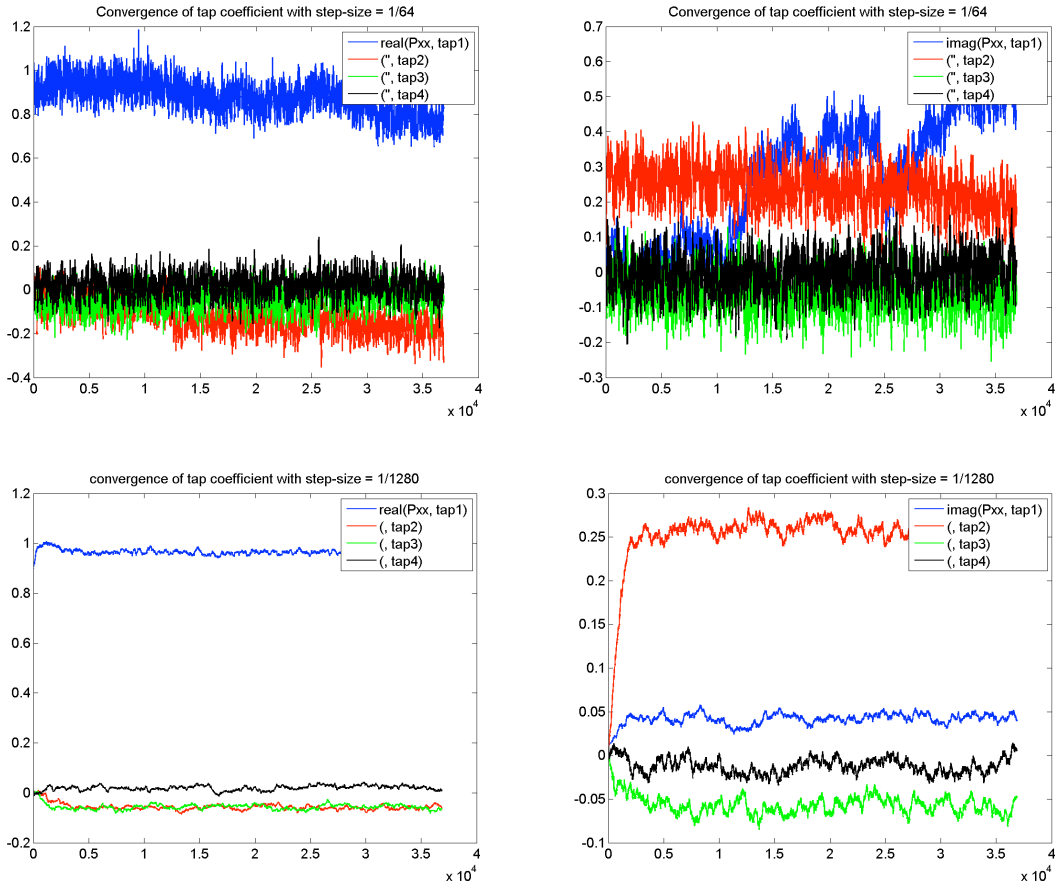

Figure 3.9 Tap convergence for step sizes 1/64 and 1/1028 in the top and bottom rows, respectively

Note in Figure 3.9, the taps for the real part of P_{xx} channel, an arbitrary, initial 'guess' is made for the tap coefficients at 0.9, 0.01, 0.01 and 0.01 for taps 1 through 4, respectively. From Figure 3.9, it is possible to see that convergence for the large step size is not realized over 4e4 iterations for the imaginary component P_{xx}, whereas for the small step size, convergence of the imaginary part is reached, albeit a non-optimal tap convergence.

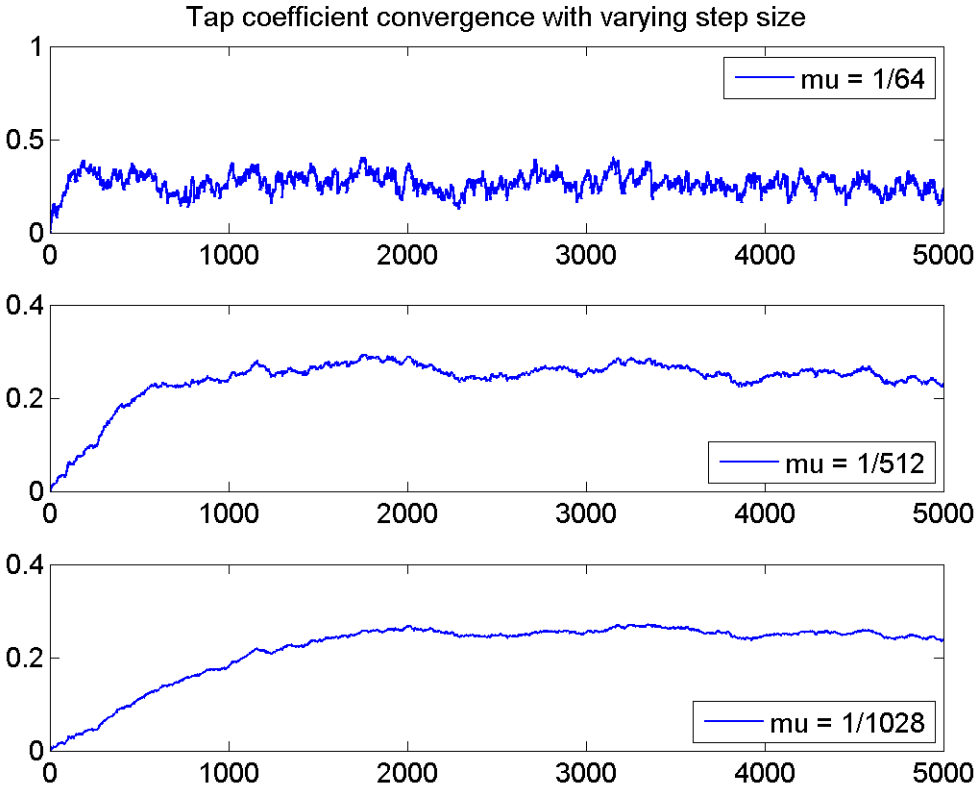

Figure 3.10. Single-tap convergence over the course of 5000 iterations for step sizes 1/64, 1/512 and 1/1028

The result for the large step size should be expected given the inability for the tap to settle at a very precise value. Should the taps ‘settle’ into convergence values for a large step size, the result is a continuing overshoot of all tap coefficients around the optimal tap coefficient values. This is more readily apparent in Figure 3.10, where a single tap coefficient is shown converging over the course of 5000 iterations.

While the *y*-axes representing the tap coefficient is not of the same scale, upon closer examination, it is evident that the smaller step size offers a definite improvement in precision over a larger step size. However, as with a smaller step size, a greater number of iterations is required if the initial guess is far off the tap coefficient producing optimal system performance. The 1/1028 step size demands the greatest number of iterations in order to attain a steady state. Should the fiber channel fast and slow axes vary drastically in rapid succession, the small step size delay filter convergence and thus cause erroneous bit recovery endlessly while the filter attempts to compensate for the rapid change in fiber characteristics.

Next, consideration is given to the CMA-FFE receiver performance when the moving average method is implemented. The benefit of the moving average method is the attention to the ‘future’ bits entering the equalizer along with the bits preceding bits to determine the ‘present’ bit value by averaging the weighted value from all taps. An issue with equalization without the moving average method is the weight of the first tap coefficient. Without considering the bits to following the current bit entering the filter,

the adaptation is prone to more drastic adjustments to tap coefficients. By using the moving average method, the 'current' bit recovered is the actually the in the middle of the bits being shifted through the filter, equating sum of prior and 'following' bits weighted by each respective tap coefficient. The CMA-FFE with moving average scheme is detailed in the following Figure 3.11 and 3.12.

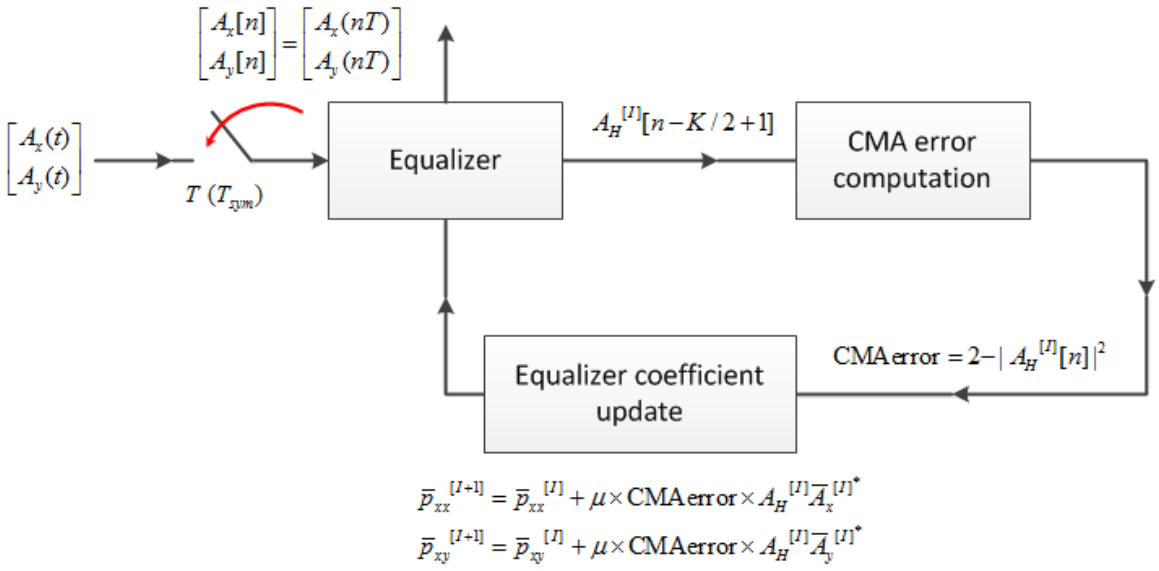

Figure 3.11. CMA-FFE with moving average setup

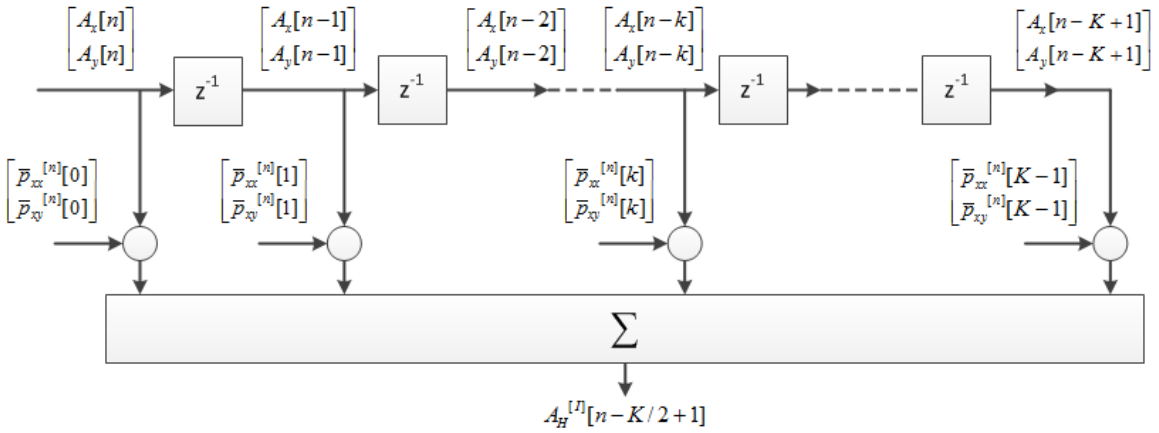

Figure 3.12. Feed-forward equalization with moving average

Again, we compare the effects of large and small step sizes. Noting that once again, the performance for a larger step size is inferior to that for a small step size in achieving tap convergence as illustrated in Figure 3.13.

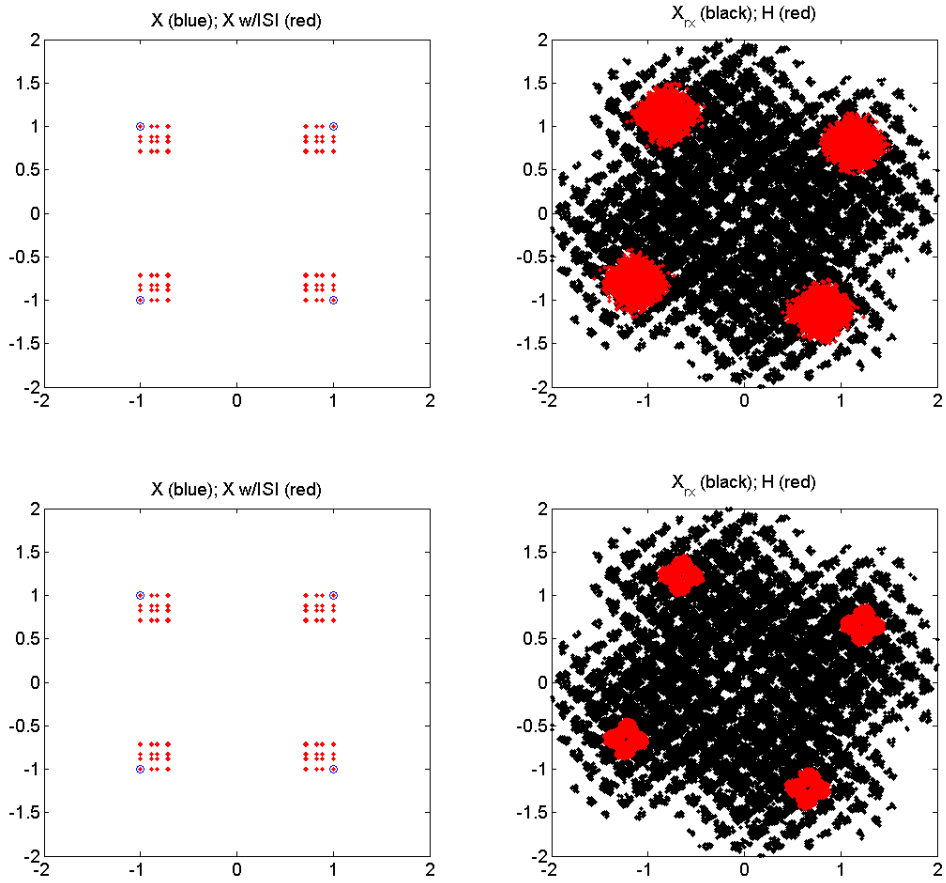

Figure 3.13. CMA-FFE with moving average with step size of 1/64 and 1/1028 in the upper and lower rows, respectively

While we do not illustrate the result here, the 20-bit sequence error performance is the same for both step-sizes with slightly lesser amplitudes for the improperly equalized bits. One again, this is does not translate directly to the performance of the system in practice.

Here, we did not simulate the additional DSP required to adjust for the rotation of the constellation map. In practice, this rotation is not variable and is readily correctable with simple DSPs. The convergence follows the same convention revealed in the results for CMA-FFE without moving average. Of greater interest is perhaps how CMA-FFE with moving average performs against that without. We consider the convergence for a single tap with the moving average method in Figure 3.14.

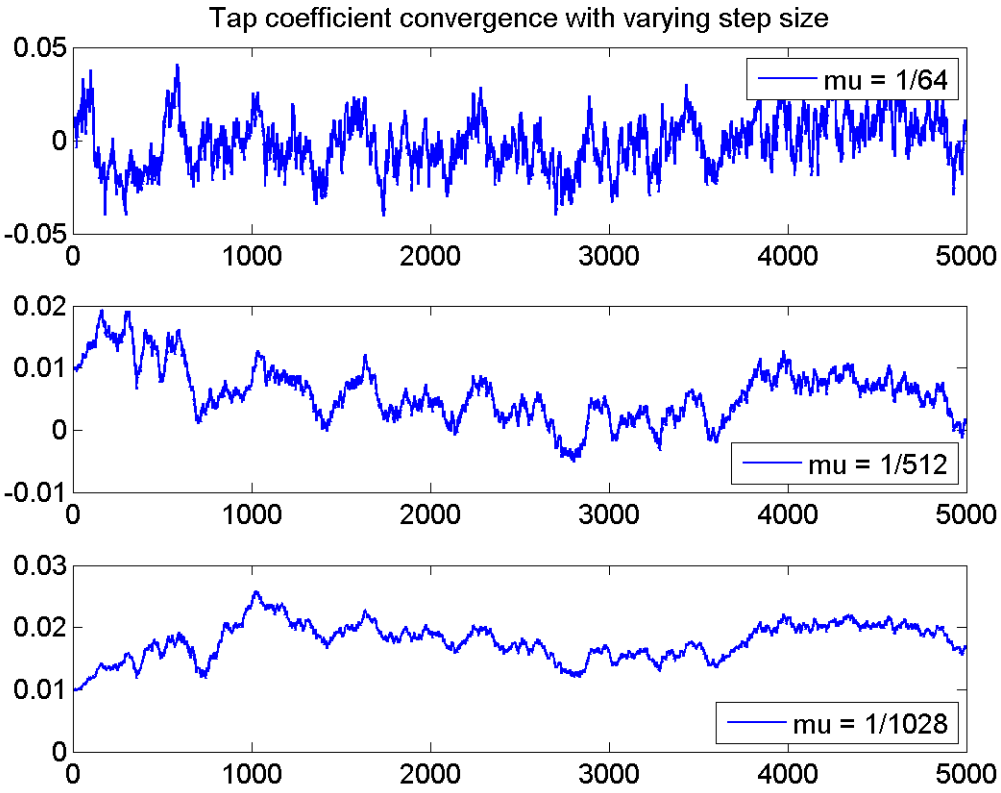

Figure 3.14 Single-tap convergence for CMA-FFE with moving average

We are able to see that the 1/64 step-size increments around 0 with a range less than 0.1 amplitude, whereas in Figure 3.10, the increments cover perhaps a 0.2 peak-to-peak

amplitude. Furthermore, precision in the moving average case is improved for the small step size μ = 1/1028. In the moving average case, the small step size illustrates convergence with the tap coefficient settling at 0.02±0.01 amplitude, whereas without moving average, the variation is greater as evidenced in Figure 3.10 where the small step size tap coefficient settles around 0.25±0.1 amplitude. In Figure 3.15, we compare CMA-FFE with and without the moving average method for small step size 1/1028.

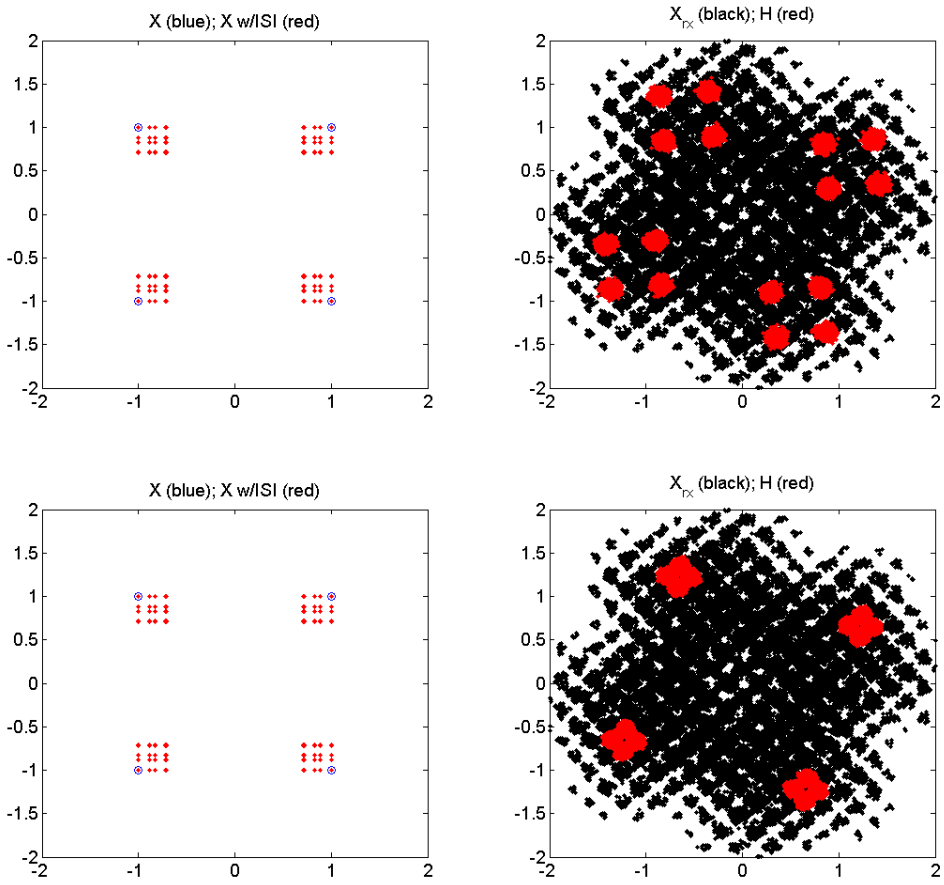

Figure 3.15. CMA-FFE performance with and without moving average in the top and bottom rows, respectively

The precision of the constellation map for the CMA-FFE with moving average is noticeably improved over that without in Figure 3.15. However, to elicit even better system performance, the number of taps may be increased in the equalizer to help compensate for ISI spread across a greater number of bits. The tradeoff for using a greater number of taps, K, is the higher computational demand within the DSP. We observe the effect of using $K = 4$ versus $K = 8$ taps for the CMA-FFE with moving average in Figure 3.16.

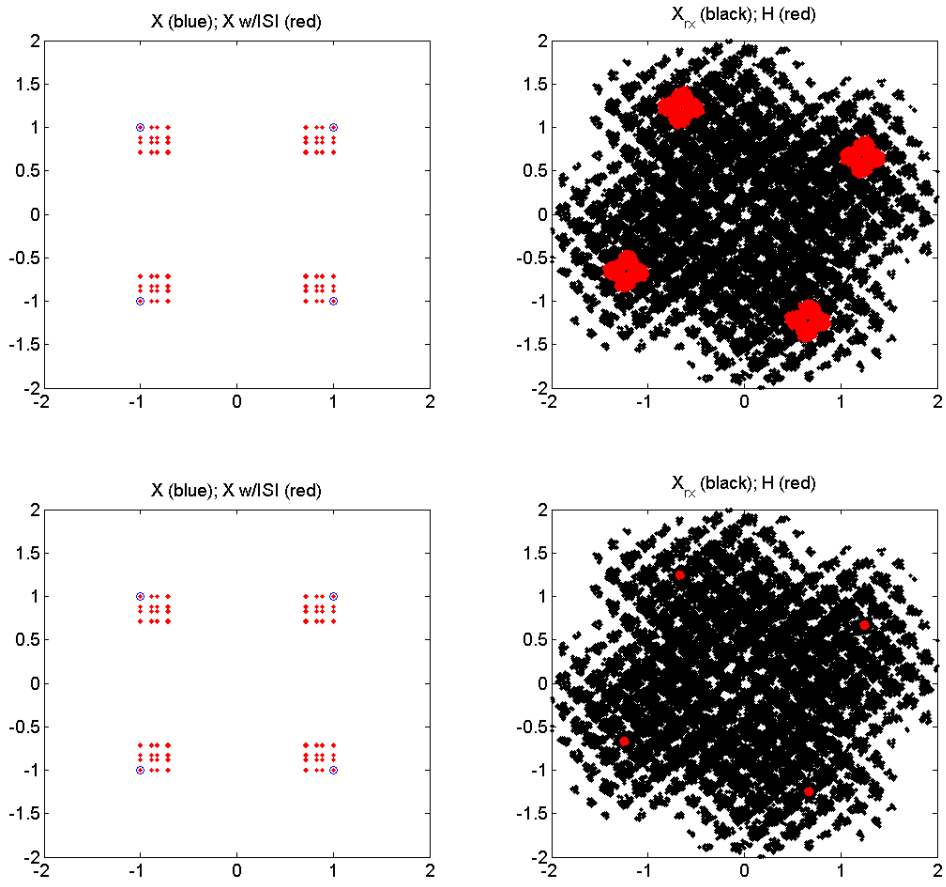

Figure 3.16. CMA-FFE with moving average with $K = 4$ and $K = 8$ taps in the top and bottom rows, respectively

As is evidenced in the constellation diagrams in Figure 3.16, the higher tap number $K = 8$ produces very high precision in state of polarization recovery, allowing for enhanced decision-directed carrier recovery. A stark contrast is evident in the ambiguity seen in Figure 3.6 for FFE-CMA without moving average equalization ($K = 4$ taps, large step size $\mu = 1/64$) as compared to FFE-CMA with moving average equalization and higher tap number K ($K = 8$, $\mu = 1/1028$).

In all constellation diagrams shown, the inability to bring about perfect carrier recovery produced a fixed rotational offset. This phase error-caused rotational offset is attributed to the ISI accumulated over the simulated span. It is critical that the phase error be within reason so that the phase is correctly identified during carrier recovery. Note that the symbol constellation for the CMA-FFE without the moving average method is significantly more ambiguous than the CMA-FFE with moving average and higher tap number.

3.7 CONCLUSIONS

As we have illustrated above, the DP-QPSK format using digital coherent detection with CMA-FFE is a viable system scheme regarding its ability to overcome ISI as well as CD and PMD for carrier recovery. We varied parameters within the equalizer such as tap number, step size and application of the moving average method and visually inspected their effect upon system performance. Computational efficiency is a concern for coherent detection, and as such, concessions must be made to establish a proper equalization and carrier recovery DSP without limiting system performance on the part of BER and bit

rate. We have offered a glimpse into the impact of these various parameters, and as expected, higher precision is afforded by a greater number of taps, smaller step size, and inclusion of the moving average method. The next logical step will be to quantitatively establish the BER of each of these parametric combinations for evaluation of the feasibility of the DSP in hardware.

Chapter 4

Summary and Future Work

As the demands for high performance cellular communications and cloud computing continue to grow rapidly, fiber optic communications systems must continually evolve and achieve ever greater efficiency to outpace the enduring upsurge in internet protocol traffic. The evolution of WDM systems from four or eight 2.5 Gb/s channels with 20 Gb/s capacity in 1995 to 80 or more 10 Gb/s channels with 1 Tb/s capacity by the year 2000 offers a glimpse of the breathtaking advancements in system capabilities over a short time span [10]. The expectation for the next decade is the commercial availability of systems operating with 100 Gb/s channels with 10 Tb/s capacity in the next year or two. Following the same tenfold improvement from the year 2000, the system specifications to be achieved by the end of this decade are 1 Tb/s channels with 100 Tb/s capacity.

To attain such imposing specifications, pioneering modulation formats must be incorporated into commercial systems in order to maintain or better system performance and elevate transmissions speeds. Legacy OOK format systems based upon a purely intensity-modulated and direct-detection scheme are being replaced by phase-modulated formats such as the balanced-detection DPSK that offer a near-twofold increase in OSNR performance. At present, the incoherent RZ-PDPSK format, effectively a DPSK scheme

with performance optimizations brought on by pre-emphasis to the electrical drive path, developed by the Oclaro group holds an 80% market share in fiber optic communications systems. Here, we thoroughly and quantitatively evaluated the performance of the RZ-PDPSK format by developing a simulation environment for a back-to-back system model.

To objectively compare this format to the standard DPSK format, several pre-emphasis levels were used in comparison with the same setup without pre-emphasis, and the system was optimized using the pre-emphasis levels in conjunction with a range of FSR bandwidths for the receiver end DLI. The purpose of this study was to determine the effect of these optimizations to improve system performance in under strong optical filtering conditions, simulating multiple OADM sites over a long haul fiber channel. We found the system optimization to return a 0.5 dB OSNR performance enhancement of pre-emphasis with FSR adjustment for the RZ-PDPSK over standard RZ-DPSK. However, back-to-back systems or systems spanning short distances with weak optical filtering do not stand to benefit substantially from pre-emphasis and FSR bandwidth tuning. Rather, fixing the DLI FSR to the bit rate produces optimal system performance.

In the second segment of our study, we considered the coherent DP-QPSK scheme. With advancements in analog-to-digital conversion electronics, ADC performance at speeds greater than 10 Gsample/s have been achieved [19]. This has led to renewed interest in coherent detection due to potential deployment on links with fibers lacking inline dispersion compensation. Studies have demonstrated QPSK encoding to offer greater

tolerance of CD and PMD. However, various DSPs have been investigated to determine an effective digital coherent detection scheme enabling optimal carrier recovery. In our study, we investigate the CMA utilized in a FFE structure with and without the moving average method for carrier recovery. We have demonstrated that the CMA-FFE with moving average can produce a very precise symbol constellation for long haul fiber optic systems with dispersive effects with a greater number of taps and smaller step size for tap coefficient adaptation.

In the future, a more rigorous, quantitative study of the coherent DP-QPSK would be beneficial to optimize the DSP to achieve a high degree of accuracy in carrier recovery while attaining the speeds necessary to reach system next-generation system specifications and maintain an acceptable BER performance. Due to the heavily computational nature of these DSPs, concessions must be made in order to ensure transceiver operation at the ultra-high speeds with a reasonable BER.

As hardware improvements continue, the varying possibilities for coherent detection are persistently explored to improve upon spectral efficiency. In particular, 16 QAM has garnered significant attention due to a twofold mprovement in spectral efficiency over DP-QPSK followed by consideration of another twofold improvement to yield 256 QAM [10, 20]. At present, the difficulties associated with the 16 QAM scheme are being sorted out. In particular, ISI is a more prominent issue due to the decreased symbol margin associated with high spectral efficiency [20]. In addition, the effects of CD and PMD must also be reduced alongside maintaining a reasonable symbol margin. Following our

study of DP-QPSK, developing a simulation environment to test a 16 QAM model with suitable equalization and carrier recovery is a logical next step in our research for the future.

LIST OF ACRONYMS

ASE	Amplified spontaneous emission
BER	Bit-error rate
BPF	Band-pass filter
BPSK	Binary phase-shift keying
CD	Chromatic dispersion
CS-RZ	Carrier-suppressed return-to-zero
CW	Continuous wave
DLI	Delay-line interferometer
DPSK	Differential phase-shift keying
DQPSK	Differential quadrature phase-shift keying
EDFA	Erbium-doped fiber amplifier
ISI	Inter-symbol interference
LPF	Low-pass filter
MZM	Mach-Zehnder modulator
NRZ	Nonreturn-to-zero
OOK	On-off keying
OSNR	Optical signal-to-noise ratio
PRBS	Pseudo-random bit sequence
QAM	Quadrature-amplitude modulation
QPSK	Quadrature phase-shift keying
RZ	Return-to-zero
SOP	State of polarization

WDM	Wavelength-division multiplexing

REFERENCES

[1] X. Zhang, X. Yi, X. Liu, P. J. Winzer, "100G transport systems: technology benchmark testing in China and evolution to terabit/s interfaces," in *China Communications*, vol. 10, no. 4, pp. 19-30.

[2] S. K. Korotky, "Traffic trends: drivers and measures of cost-effective and energy-efficient technologies and architectures for backbone optical networks," in *OFC/NFOEC*, Los Angeles, CA, Mar. 2012, pp. 1-3.

[3] J. Kaur, N. Sharma, "Effects of amplified spontaneous emission (ASE) on NRZ, RZ and CSRZ modulation formats in single channel light-wave systems," in *ETNCC*, Udaipur, IN, Apr. 2011, pp. 61-64.

[4] G. P. Agrawal, Fiber-Optic Communication Systems, 4th ed. Wiley, 2010.

[5] A. H. Gnauck, P. J. Winzer, "Optical phase-shift-keyed transmission," *J. Lightwave Technology*, vol. 23, no. 1, pp. 115-130, 2005.

[6] P. J. Winzer, R. Essiambre, "Advanced optical modulation formats," in *IEEE Proceedings*, vol. 94, no. 5, pp. 952-985, 2006.

[7] R. M. Jopson, A. H. Gnauck, L. E. Nelson, L. D. Garrett, "Evaluation of return-to-zero modulation for wavelength-division-multiplexed transmission over conventional single-mode fiber," in *OFC*, San Jose, CA, Feb. 1998, pp. 406-407.

[8] P. J. Winzer, R. J. Essiambre, "Advanced modulation formats for high-capacity optical transport networks," *J. Lightwave Technology*, vol. 24, no. 12, pp. 4711-4728, 2006.

[9] X. Zhang, H. Y. Xu, H. J. Niu, C. L. Bai, "Application of DQPSK format based on CSRZ in PMD compensation," in *ICOCN*, Nanjing, CH, Oct. 2010, pp. 258-261.

[10] R. W. Tkach, "Scaling optical communications for the next decade and beyond," *Bell Labs Technical Journal*, vol. 14, no. 4, pp. 3-9, 2010.

[11] Q. Zhang, C. Huang, A. Rahman, "Performance optimization for 44 Gb/s return-to-zero partial DPSK transceiver with pre-emphasized electrical signal driving path," in *ICCC*, Beijing, CH, Aug. 2012, pp. 245-249.

[12] Q. Zhang, A. Rahman, M. A. Khaliq, H.-W. Huang, "Performance optimization for 80 Gb/s NRZ-DPSK transceiver with pre-emphasized electrical signal driving path," in *IEEE/LEOS*, Portland, OR, Jul. 2007, pp. 260-261.

[13] A. J. Seeds, "Optical transmission of microwaves," *The Review of Radio Science*, pp. 335-343, 1996.

[14] M. D. Jeruchim, P. Bababan, K. S. Shanmugan, *Simulation of Communication Systems: Modeling, Methodology, and Techniques*. New York: Kluwer/Plenum, 2000.

[15] B. Mikkelson, C. Rasmussen, P. Mamyshev, F. Liu, "Partial DPSK with excellent filter tolerance and OSNR sensitivity," *Electron. Lett.*, vol. 42, pp. 1363-1364, 2006.

[16] J. Proakis, *Digital Communications*, 5th ed. McGraw-Hill, 2007.

[17] L. W. Couch II, *Digital and Analog Communication Systems*, 7th ed. Upper Saddle River, NJ: Prentice Hall, 2006.

[18] K. Kikuchi, "Performance analyses of polarization demultiplexing based on constant-modulus algorithm in digital coherent optical receivers," *Optical Express*, vol. 19, no. 10, 2011.

[19] L. Nelson, S. L. Woodward, S. Foo, X. Zhou, M. D. Feuer, D. Hanson, D. McGhan, H. Sun, M. Moyer, M. O. Sullivan, P. D. Magill, "Performance of a 46-Gbps dual-polarization QPSK transceiver with real-time coherent equalization over high PMD fiber," *J. Lightwave Technology*, vol. 27, no. 3, 2009.

[20] M. M. H. Adib, M. I. Khalil, A. M. Chowdhury, M. S. Faruk, G. K. Chang, "Equalization and carrier recovery for 112Gbps optical coherent system with HEX-16-QAM modulation," in *ICECE*, Dhaka, BD, Dec. 2012, pp. 559-562.